https://doi.org/10.5194/egusphere-2022-180
Preprint. Discussion started: 10 May 2022

Strato-structural evolution of the deep-water Orange Basin: Constraints from high-resolution 3D seismic data

Nombuso G. Maduna[1], Musa S.D. Manzi[1], Zubair Jinnah[1], Julie E. Bourdeau[2]

[1]School of Geosciences, University of the Witwatersrand, Johannesburg, PBag 3, WITS, 2050, Republic of South Africa
[2]Geological Survey of Canada, 601 Booth Street, Ottawa, Ontario, K1A 0E8, Canada.

Correspondence to: Nombuso G. Maduna (nombuso.maduna@gmail.com)

Abstract. We use high-resolution 3D reflection seismic data to constrain the strato-structural evolution of the transitional and compressional domains of a Late Cretaceous deep-water fold-and-thrust belt (DWFTB) system and its influence on the overlying Cenozoic megasequence in the Orange Basin, South Africa. Multiple shale detachment surfaces have given rise to a complex structural framework, allowing for the redistribution of stress and strain, with progressive deformation and sedimentation. High-resolution 3D seismic data show that the compressional domain exhibits large-scale landward-dipping DWFTBs with faults mainly detaching the Turonian shale detachment surface. Thrust sheets are segmented along strike by extensive oblique-slip faults which extend from the transitional domain into the down-dip compressional domain. The transitional domain is imaged as a complex region containing listric normal, thrust, and oblique-slip faults. Many faults in the transitional domain have been reactivated to detach onto an older Albian shale detachment surface at depth, transferring stress and distributing strain during gravitational sliding. Smaller, localized fold-and-thrust belts are subsequently formed in the down-dip compressional domain directly below the kilometre-scale DWFTB system between the upper Turonian and lower Albian shale detachment surface. Mass erosional processes of the Cenozoic are confined above the transitional domain including a large, roughly slope-perpendicular Oligocene submarine canyon formed by turbidity currents, and a smaller series of slope-parallel, sinusoidal channel-like features in the Miocene formed by bottom currents. Normal and oblique-slip faults from the transitional domain have been reactivated to terminate at either one of the Oligocene or Miocene sequence boundaries. This, together with a present-day seafloor slump scar above a buried Late Cretaceous syncline, indicates how the stratigraphy and structural geometry of a buried DWFTB system controls fundamental sedimentary processes in an evolving continental margin.

1 Introduction

The southwest African coastline is a prime site for the study of processes in passive margin settings. From shallow to deep-water environments, the coastline records not only the late Jurassic to Early Cretaceous break-up of Gondwana, but also the post-rift evolution of the African margin (Fig. 1; Séranne and Anka, 2005). The gravitational collapse and subsequent contraction of sedimentary sequences in the deep ocean formed deep-water fold-and-thrust belts (DWFTBs); distal sedimentary wedges of interrelated folds, and thrust faults created over a sloping detachment surface (Rowan et al., 2004; Nemcok et al., 2005). DWFTBs form part of a linked tripartite system consisting of a: 1) down-dip compressional domain (within which DWFTBs form), 2) central transitional domain, and 3) up-dip extensional domain in proximity to the coastline (Rowan et al., 2004; Krueger and Gilbert, 2009; Morley et al., 2011). The advancement in deep-water drilling technology by the petroleum industry over the last two decades has promoted interest in the study of DWFTBs as their anticlines are known to host vast reserves of hydrocarbons (e.g., Corredor et al., 2005; Benesh et al., 2014).

Well-preserved DWFTB systems are found within the Orange Basin, along the western coastline of South Africa and Namibia (Paton et al., 2007; Butler and Paton, 2010; de Vera et al., 2010 and references therein). The DWFTB systems are classified as type 1a, near-field stress-driven systems containing multiple shale detachment surfaces with deformation driven by margin uplift and sediment loading (Morley et al., 2011; King and Morley, 2017). Although there is extensive 2D legacy seismic data coverage in the South African portion of the Orange Basin, the basin remains largely underexplored with only one well per 4 000 km^2 (Fig. 2; PASA, 2017; van der Spuy and Sayidini, 2022). In South Africa, no wells have been drilled in the most distal deep-water environments of the Orange Basin. In Namibia however, directly adjacent to this present study, Shell made a significant hydrocarbon discovery from the Graff-1 appraisal well (Fig. 2) drilled between December 2021 and February 2022 (van der Spuy and Sayidini, 2022). Considering the significant Namibian discovery, South Africa's hydrocarbon prospects are high since the two deep-water regions share a similar geology.

The use of early 2D reflection seismic data and later higher resolution 3D reflection seismic data acquired in the Orange Basin has allowed certain key elements of its evolution to be constrained through several studies (e.g., de Vera et al., 2010; Dalton et al., 2015, 2017; Collier et al., 2017; Baby et al., 2018; Mahlalela et al., 2021). These studies, the majority of which used 2D reflection seismic data since 3D seismic coverage is sparse, have described events within the late stages of continental breakup, to the formation of gravitational collapse structures (DWFTB systems) present. At present, there is a great paucity of data for the transitional domain of these systems due to its structural complexity and how it has been poorly seismically imaged (mainly 2D), thus making it difficult to interpret. This is in stark contrast to their up-dip extensional and down-dip compressional counterparts, which have been well-studied due to the simplicity of the former and known hydrocarbon potential of the latter (e.g., Paton et al., 2007, 2008; Butler and Paton, 2010; de Vera et al., 2010; Baby et al., 2018). Previous 2D seismic studies of the Orange Basin have also only shown seismic sections orientated perpendicular to the margin, which corresponds to a roughly E–W transect, recording only the proximal to distal change in margin structure and stratigraphy (e.g., Paton et al., 2007; Butler and Paton, 2010; De Vera et al., 2010; Hartwig et al., 2012; Dalton et al., 2017; Baby et al., 2018).

In this study we use high-resolution 3D reflection seismic data from the Orange Basin to provide an in-depth examination of the transitional domain from a buried DWFTB system (Fig. 2). We define its relationship to the down-dip compressional domain and assess how both domains have structurally affected the younger deposits with progressive sedimentation. We also look at the along-strike change in stratigraphy and structure of both domains along the margin. From these observations we create a model describing not only the evolution of one DWFTB system, but also that of the overlying passive margin sediments as the DWFTB system played a significant role in deforming the overlying stratigraphy.

2 Regional setting

The Orange Basin is located off the SW coast of Africa and covers an extensive area of approximately 160 000 km^2, including the Namibian extension, making it South Africa's largest offshore basin both aerially and volumetrically (Kuhlmann et al., 2010; PASA, 2017). It has acted as the depocentre for sediments deposited from the Olifants and Orange rivers since the Lower Cretaceous (Maslanyj et al., 1992; De Vera et al., 2010).

2.1 Offshore structural framework

The offshore structure of the SW African coastline has undergone two major phases of deformation. This includes: 1) Basin and Range type extension and rifting during the Middle to Late Jurassic breakup of Gondwana; followed by 2) thermal subsidence at the onset of continental drift with the development of a passive margin during the Late Cretaceous to early Palaeogene (Maslanyj et al., 1992; Light et al., 1993; Clemson et al., 1997; Hartwig et al., 2012). As in all margins, very little is known of the SW African margin's configuration prior to rifting (Mohammed et al., 2017). What is known is that the pre-rift basement forms a 30 km wide, N-S orientated zone of pronounced flexure induced by thermal subsidence in the continental lithosphere (Light et al., 1993; Clemson et al., 1997; Mohammed et al., 2017; Baby et al., 2018). This zone, known as the hinge line, has separated regions of subsidence with regions of stasis or uplift ever since the Mesozoic, forming a critical boundary of the margin's offshore and onshore morphologies (Light et al., 1993; Clemson et al., 1997; Aizawa et al., 2000). The hinge line is offset by several structurally different, along-strike segment boundaries which partitioned the timing of rifting in Gondwana break-up (Clemson et al., 1997).

The first phase of deformation, extension and rifting, is characterized by the offshore north-south structural grain and east-west orientated fracture zones accommodating the development of three main Lower Cretaceous depocentres (Light et al., 1993). These depocentres mark, from south to north and hence oldest to youngest, the position of the Orange, Lüderitz and Walvis basins which formed in zones of subsidence (Fig. 1). The basins are contained between the Rio Grande Fracture Zone to the north, and the Aghulhas-Falkland Fracture Zone to the south, which enabled right-lateral (dextral) strike-slip motion during rifting (Fig. 1; Séranne and Anka, 2005). Lesser depocentres offshore the southern tip of South Africa accommodated the formation of the smaller Cape and Outeniqua basins. The second phase of deformation, drift, is correlated to the onset of a spreading oceanic ridge which subdivided the margin into well-defined shelf, slope and basinal environmental settings (Light et al., 1993; Séranne and Anka, 2005). The region has experienced moderate seismic activity through earthquakes which may be responsible for triggering lower slope turbidites as seen along the SE margin of South Africa (Rogers and Rau, 2006).

2.2 Offshore stratigraphy

The offshore stratigraphy of SW Africa is described in terms the two major phases of deformation that affected the margin; the syn-rift succession comprises of sediments deposited during margin extension and rifting, and the post-rift succession comprises of sediments deposited from the beginning of drifting until present (Fig. 3; e.g., De Vera et al., 2010). Sedimentation and facies distribution were tectonically controlled in the deposition of the syn-rift succession (Light et al., 1993), which forms a megasequence of Late Jurassic to Early Cretaceous (late Hauterivian) siliciclastic and volcaniclastic sediments (Fig. 3, Paton et al., 2008; Dalton et al., 2017). The syn-rift succession is a classic example of a volcanic rifted margin setting with seaward-dipping reflectors (Maslanyj et al., 1992; Menzies et al., 2002). Overlying and separated from this succession, via a regional break-up unconformity, are the Late Hauterivian (Early Cretaceous) to present-day clastic sediments of the post-rift succession (Fig. 3, Light et al., 1993; Menzies et al., 2002; Granado et al., 2009). The main factor which influenced sedimentation and facies distribution in the post-rift succession were eustatic sea-level changes (Light et al., 1993).

The 130 Ma to present day post-rift clastic sediments, largely sourced from the Olifants and Orange river systems and their ancestral equivalents, reach a central basin thickness of 3 km in the south and 5.6 km in the north of the Orange Basin (Paton et al., 2008; Granado et al., 2009; Dalton et al., 2017). Dalton et al. (2017) subdivide the post-rift succession into three megasequences; early drift (Early Cretaceous), late drift (Late Cretaceous) and Cenozoic. The early drift megasequence is comprised of black shales and claystones. The late drift megasequence, within which most gravity collapse structures are found, is comprised of interbedded heterolithic shales and claystones. The post-rift stratigraphy of the Orange Basin has been well-described by many authors (e.g., Emery et al., 1975; Bolli et al., 1978; Brown et al., 1995; Holtar and Forsberg, 2000; Paton et al., 2008; Granado et al., 2009; De Vera et al., 2010; Kuhlmann et al., 2010; Dalton et al., 2017; Baby et al., 2018) who subdivided the succession into several stratigraphic units (sequences) separated by key stratigraphic markers or bounding surfaces (Fig. 3). The nomenclature of stratigraphic markers range between different authors with the most widely used being those of Brown (1995) for the Lower and Late Cretaceous (Fig. 3).

3 Data and methods

3.1 Acquisition

Shell Global Solutions International commissioned a high-resolution 3D seismic survey between 2012–2013 in the deep-water Orange Basin (Kramer and Heck, 2014). The survey acquisition parameters are summarised in Table 1. The survey covers a total area of ~ 8 200 km^2 with the survey designed in a ~ NNW to SSE orientation (Fig. 2b). However, for the purpose of this study, we report only the results covering an ~1 800 km^2 portion of the full seismic dataset (Fig. 2b). The survey used dual airgun arrays with a source volume of 0.0672 m^3 towed at 8 m depth with a 25 m shot point interval, and a 7950 m long streamer with a 12.5 m group interval and 12.5 m group length. The data were recorded at a 2 ms sample rate for a total record length of 7168 ms. A low-cut frequency of 4.4 Hz at a 12 db/Oct slope and a high-cut frequency of 214 Hz at a 341 db/Oct slope were used during data acquisition giving a dominant frequency of 50 Hz after the application of an anti-aliasing filter.

3.2 Seismic processing and interpretation

Pre-processing from field tape seismic data was first carried out onboard by the Dolphin Geophysical Polar Duchess. This involved data conversion from SEG-D to SEG-Y output. The full processing was carried out at 4 ms from SEGY field tape data through surface-related multiple elimination (SRME) using 3D SRME and anisotropic Kirchhoff pre-stack depth migration (PreSDM) (Table 2). In this study the data is geologically interpreted using the Petrel Schlumberger software. Using velocities from Kuhlmann et al. (2010) and Mahlalela et al. (2021), depth conversion was carried out using the interval velocity model; 1 800 ms^{-1}, 2 000 ms^{-1}, 2 000 ms^{-1} and 4 500 ms^{-1} velocities were used for the seafloor, Oligocene, and Albian surfaces (as named in this study), respectively. The full workflow is shown in Fig. 4 to build a 3D geological model.

3.2.1 Seismic resolution limit

With a dominant frequency of 50 Hz and average velocity of 2 400 ms^{-1} reported for the study area, the vertical seismic resolution limit given for the ¼ (Yilmaz, 2001) and $^1/_8$ (Widess, 1973) dominant wavelength criteria is 12 m and 6 m, respectively. The horizontal seismic resolution limit is calculated from the radius of the Fresnel Zone which is ultimately determined by the wavelength (Yilmaz, 2001). For migrated data, the horizontal resolution collapses to half the dominant wavelength. With a dominant wavelength of 48 m for our seismic data, the horizontal resolution limit is 24 m. Geological features smaller than the vertical and horizontal resolution limits are indistinguishable. It is only through the application of seismic attributes that features lower than the resolution limit may be detected. An example of this is presented in Manzi et al. (2013) where they detected more fine-scale structures in a Witwatersrand gold mine than previously known.

3.2.2 Structure delineation using seismic attributes

Seismic attributes are designed through mathematical manipulation of the seismic data. They are often used to enhance important geological and physical properties of the seismic data by delineating of faults, resolving thin beds, and identifying bright spots that could correspond to hydrocarbon reservoirs (Chopra and Marfurt, 2005, 2007; Brown, 2011). Seismic attributes are dependent on the signal-to-noise (S/N) ratio of the data and therefore need to be conditioned using various filters. Schlumberger's Petrel software offers a wide variety of seismic attributes which may be applied on the whole volume or on interpreted horizons. Volumetric attributes may be applied from the onset of seismic interpretation to the entire volume while horizon-based attributes are only appliable once sufficient interpretation has taken place on a surface of interest (Brown, 2011).

Structural smoothing was first applied to the full seismic volume to condition the data. It is used to increase the S/N ratio by smoothing the seismic data's input signal through local averaging with a Gaussian filter (Randen et al., 2000). Using the structurally smoothed volume as input, the variance attribute was applied to enhance fault discontinuities throughout the seismic section. Variance is an attribute that measures the local deviation of the seismic signal in the form of a coherency analysis (Silva et al., 2005), and is used in many studies (e.g. Maselli et al., 2019) to highlight faulted areas in place of the similar chaos attribute.

To further enhance fault continuities and visualise 3D geometric variations, horizon-based attributes such as edge detection and influential data were applied to surfaces of interest. Horizon-based attributes were used in conjunction with the surface smoothing structural operation which filters out anomalous peaks from picking. Edge detection extracts an edge model to enhance discontinuities by combining the dip and dip azimuth properties and normalizing these to the local noise of the surface

(Randen et al., 2000; Manzi et al., 2012). Influential data generates a property on the data object that highlights areas of rapid 3D geometric variation which is key to ensuring sensible geometric form.

4 Results and interpretations

The study area lies along the continental slope between water depths of 1 000 to 2 000 m, bordering the Namibian licensing area (Fig. 2). This study's seismic volume images the compressional and transitional domain of the Late Cretaceous DWFTB system (Fig. 5) together with the overlying Cenozoic megasequence. The seismic stratigraphy and structural framework of each domain and their overlying sediments is described and seen from three regional sections; Figs. 6, 7 and 8, the location of which are shown in Fig. 5. Table 3 summarizes the observations and interpretations of all seismic sections including each stratigraphic sequence and the stratigraphic markers/bounding surfaces that separate them.

Figure 6 is a full crossline section of the study area, showing a portion of the transitional domain and, more importantly, the compressional domain. The regional section lies roughly perpendicular to the DWFTBs giving a clear view of their internal geometry and surroundings. We also examine the along-strike component of the compressional and transitional domains in Figs. 7 and 8, respectively, since it is often always neglected. Figure 7 is an inline section orientated roughly parallel to the DWFTBs and perpendicular to the normal and oblique-slip faults (see Fig. 5). Figure 8 is an inline section of the distal-most transitional domain reflecting its stratigraphy and that of the overlying sediments it has affected. Results and interpretations for the seismic stratigraphy and structural framework observed throughout the study are described below

4.1 Seismic stratigraphy

Stratigraphic markers are surfaces that subdivide the sedimentary succession into interpretable stratigraphic sequences based on internal configuration patterns. Stratigraphic markers were picked because of their dominant high amplitude reflections observed laterally throughout the seismic section. We identified nine key seismic stratigraphic markers in this study which coincide with major geological events recognized in the Orange Basin described by various authors (Fig. 3; Brown et al., 1995; Paton et al., 2008; De Vera et al., 2010; Kuhlmann et al., 2010; Hartwig et al., 2012; Dalton et al., 2017; Baby et al., 2018). Figure 3 shows how the nomenclature used for the stratigraphic markers and stratigraphic sequences have differed between various authors, however the most commonly used nomenclature for stratigraphic markers are those of Brown et al. (1995).

To avoid confusion in this study, we simply named our stratigraphic markers, 1–9, according to the geological time we postulated from the combination of studies by Brown et al. (1995), Dalton et al. (2017), and Baby et al. (2018) (Fig. 3 and Table 3). From oldest to youngest these are the: 1) Albian (14At1), and uninterpreted 2) Turonian (15At1) maximum flooding surfaces (MFSs); the 3) Santonian (~16Dt1), 4) early Campanian (17At1), 5) late Campanian (18At1), 6) Maastrichtian (22At1), 7) Oligocene and 8) Miocene unconformities; and 9) the seafloor (Figs. 3 and 9). The second oldest surface, the

Turonian (marker 2 and the 15At1), was omitted from seismic interpretation and modelling in the Petrel software (Fig. 9) due to its discontinuous nature in areas of the seismic section seen in Figs. 7 and 8.

The nine stratigraphic markers are bounding surfaces to nine stratigraphic sequences identified in the study (Table 3 and Figs. 6, 7 and 8). In this study, the stratigraphic sequences have been grouped into four megasequences (A–D; Fig. 3) reflecting the three major phases of margin evolution (early drift, late drift and Cenozoic) first described in Dalton et al. (2017). The sequences are subdivided as follows, beginning from the mid-Early Cretaceous: early drift (A), late drift (B1–C3), and Cenozoic (D1–D3). Older stratigraphic markers and sequences (below the Albian) were left uninterpreted since most lie below the vertical extent of the seismic volume and were cut off (Figs. 6, 7 and 8).

4.1.1 Early drift megasequence (A)

A is an approximately 400–700 m thick sequence characterized by low to medium amplitude, chaotic (Fig. 8), subparallel to mounded, internal reflections (Figs. 6 and 7). The sequence is bound between two medium amplitude upper (marker 1) and lower stratigraphic markers, the latter of which remained uninterpreted as explained in the section above. The upper stratigraphic marker, 1, is interpreted as the Albian maximum flooding surface (Table 3). It also a shale detachment surface upon which some faults terminate at depth as discussed later in the structural framework (Section 4.2).

4.1.2 Late drift megasequence (B1-C3)

B1 is a 0–500 m thick sequence characterized by deformed, medium to high amplitude, chaotic and mounded internal reflectors (Figs. 6, 7 and 8). The strongly mounded geometry, well shown in in Fig. 8, reflects basin floor sediments of the transitional domain. The upper bounding surface, marker 2, is interpreted as the Turonian shale detachment surface upon which most faults terminate (Section 4.2) and a maximum flooding surface. This thick, medium to high amplitude surface is undulatory and irregular due to the deformation of the overlying and sequences (Fig. 6). It often merges with the underlying Albian surface (marker 1) (Fig. 8). The Albian (marker 1) and Turonian (marker 2) shale detachment surfaces are the 14At1 and 15At1 surfaces referred to in literature (Brown et al., 1995; Paton et al., 2007, 2008; Kuhlmann et al., 2010; Dalton et al., 2017; Baby et al., 2018).

Sequence B2 is a sedimentary wedge that thickens from 900–1 700 m progressing seawards in the down-dip direction, with the greatest thickness in the central region of the entire seismic volume shown in Figs. 6 and 7. The sequence is characterized by deformed, medium to high amplitude seismic reflections. The internal geometry in the compressional domain appears as stacked, steeply NE-dipping reflections (Fig. 6) which flatten towards the transitional domain to become parallel with the underlying and overlying sequences (Fig. 8). The steeply dipping reflections are folded into asymmetric anticlines distinctly separated by imbricate thrusts creating fold-and-thrusts (Section 4.2; Figs. 6 and 9). The gradual thickening of sequence B2 from the transitional to the compressional domain, observed in Figs. 6 and 10, was caused by the downslope compression of sediment. The upper bounding surface of sequence B2, marker 2, is interpreted as a Santonian surface that defines the main crest of the kilometre-scale DWFTBs. It is a thick, high amplitude surface conformable to the folded geometry of the sequence. Figure 10 is a 3D seismic section showing sequences A to B2 capped by the Santonian surface. The horizon-based attribute of dip angle was computed for the surface to enhance the morphology of the fold crests dipping between 0–15°. A large syncline is imaged in sequence B2 (NW portion of Fig. 7) which affected more recent seafloor deformation (Section 4.1.3).

C1 is a sedimentary wedge that thins from 1 000 m in the transitional domain to 120 m in the distal contractional domain (Fig. 6). It is characterized by low amplitude, concave-upwards sag geometries that onlap and downlap the Santonian surface (marker 2) (Figs. 6, 7 and 8). In the more distal region of compressional domain however, the reflectors have stacked conformably with the underlying sequence (SW portion of Fig. 6). Stratigraphic marker 4 is the upper bounding surface of sequence C1. It is interpreted as the early Campanian sequence boundary since it erosionally truncates the sequence (Figs. 6 and 7).

Compared to the underlying B2 sequence, C1 is weakly folded with smaller thrust displacements suggesting a syn-kinematic relationship whereby thrusting was still active and contemporaneous with the deposition of sequence C1. The thick B2 and C1 sequences (Figs. 7 and 8) indicate a large increase in sediment supply during the Coniacian to early Campanian (Late Cretaceous). This, together with the onlap and downlap (NW portion of Fig. 7) of sequence C1 reflections against the Santonian surface (marker 3), indicate a localized increase in accommodation space above the transitional domain during the downward compression and translation of sediment (Fig. 6). Onlap also implies greater deformation than sedimentation rates (Dalton et al., 2017).

C2 is a ~200 m thick sequence of thin, wavy to parallel, high frequency, high amplitude seismic reflectors (Figs. 6, 7 and 8). Reflectors are initially wavy at the base of the sequence, due to folding above the underlying thrust planes, then gradually straighten to parallel continuous reflections at the top of sequence C2 (Figs. 6 and 7). The sequence's upper bounding surface (marker 5) is a thick, very high amplitude conformable surface interpreted as being late Campanian maximum flooding surface. The change in geometry of sequence C2 reflections indicates a gradual decrease in the rate of deformation relative to sedimentation suggesting downslope thrusting ended by the end of the late Campanian.

Sequence C3 thins seawards from 200–90 m forming a wedge-shaped package (Figs. 6, 7 and 8). The internal geometry consists of thick, parallel, very high amplitude seismic reflectors, including that of its upper bounding surface (marker 6) interpreted as the conformable Maastrichtian maximum flooding surface.

Sequences C1 and C3 consist of seawards-thinning wedges of sediment (Fig. 6) that indicate a gradual decrease in sediment supply distally along the continental slope. Stratigraphic markers 3–6 which are the Santonian, early Campanian, late

Campanian and Maastrichtian surfaces are a combination of sequence boundaries (erosional surface separating depositional cycles) and maximum flooding surfaces (Baby et al., 2018). The more dominant type of surface is referred to in Table 3.

It was difficult to constrain the exact age of stratigraphic markers 3, 4, 5 and 6 tentatively assigned the; Santonian (16Dt1), early Campanian (17At1), late Campanian (18At1) and Maastrichtian (22At1) ages, respectively, according to the nomenclature originally proposed by (Brown et al., 1995). Brown et al. (1995) and other Orange Basin studies (e.g. Paton et al., 2007, 2008; Kuhlmann et al., 2010; Dalton et al., 2017; Baby et al., 2018) who likewise identified and interpreted these surfaces, were constrained by the use of 2D reflection seismic data (except Kuhlmann et al., 2010) limited to the proximal, shallower regions of the basin (except Dalton et al., 2017). In passive margin settings not all surfaces found in the proximal regions will be found in the more distal reaches since sediment supply decreases oceanward; surfaces thin out and eventually disappear, appearing to combine with an underling surface. This is seen in our deep-water 3D seismic study (Fig. 6) and must also be the case when comparing the shallow to deep-water extents of the Orange Basin.

4.1.3 Cenozoic (D1-D3)

Influential data and edge detection horizon-based attributes were used to enhance the 3D geometric variation of erosional features observed upon the Oligocene and Miocene (Cenozoic) sequence boundaries (Fig. 11). The lowermost Cenozoic sequence corresponds to the D1 retrogradational sequence, forming a 450–100 m seaward-thinning wedge (Fig. 6). It is characterized by low amplitude, parallel seismic reflections which downlap the Maastrichtian (marker 6) maximum flooding surface mostly in the transitional domain (Fig. 8). Sequence D1 (and a small upper portion of the underlying C3 in the transitional domain, Fig. 8) is erosionally truncated by a SE–NW trending submarine canyon running perpendicular to the slope (Fig. 11a, b) referred to as the Oligocene sequence boundary or subaerial unconformity surface (marker 7). The canyon is situated above a ~1.3 km wide horst from the Late Cretaceous B2 sequence with opposite dipping normal faults in the transitional domain (Fig. 8). The horst forms a large anticline with chaotic internal reflectors observable in sequence B2 and outlined in Fig. 8. The canyon is ~2.3 km wide with a visible length of 13 km length, which extends beyond the seismic dataset proximally (Fig. 11a, b). Onlapping against the walls of the canyon and overlying the Oligocene subaerial unconformity (marker 7) is the 100–200 m thick D2 sequence (Fig. 8). It comprises low amplitude, parallel reflectors with some chaotic sections, indicative of reworked sediment by turbidity currents. More than one erosional event is evident both before and after the main Oligocene unconformity surface as reflectors within sequences D1 and D2 have been erosionally truncated.

Stratigraphic marker 8 is a medium to high amplitude surface, referred to as the Miocene sequence boundary which cuts the upper D2 reflectors (Fig. 8 and 11c, d). It is an irregular subaerial unconformity characterized by a series of multiple NW–SE trending, sinusoidal crosscutting channels (Fig. 11c, d). The channels trend parallel to the continental slope and are ~500 m in width. The large extent of crosscutting and overlapping makes it difficult to differentiate between individual channels and their lateral extents.

Sequence D3 is the youngest Cenozoic, and therefore uppermost, sequence. It forms a 100–350 m seaward thickening wedge (Fig. 6) characterized by medium to low amplitude, mounded to parallel reflectors. The earliest sediments of the sequence are mounded in geometry for approximately 80 m till later sediments were deposited continuously in a parallel manner (Figs. 6 and 7). Stratigraphic marker 9 is the present-day seafloor, a very high amplitude and thick surface. Slumping, characterized by chaotic internal reflectors, is evident on the present-day seafloor (seen in NW of Fig. 7 and a portion of Fig. 9). The slump scar is ~7 km in width, sitting directly above the region of a large Late Cretaceous syncline (B2 sequence) (Fig. 7).

4.2 Structural framework

The sedimentary succession comprises several sedimentary packages displaced by a complex structural framework of faults as shown in Figs. 5, 9 and 12. Figure 5a shows the variance attribute in TWT at time slice -3 424 ms which was used to enhance the lateral continuity of faults. The variance time slice sits within sequence B2, covering depths approximately between -3 200 m to -5 000 m of the sloping stratigraphic column (Figs. 6, 7 and 8). The chaos volumetric attribute, was used over the variance attribute in an adjacent Orange Basin study to show the vertical continuation of thrust faults from the Late Cretaceous to the lower Cenozoic megasequences (Mahlalela et al., 2021). Figure 5b combines the interpretation of the variance attribute time slice (Fig. 5a), the Santonian surface (marker 3) (Fig. 10) and the dip directions of the fault framework observed in Fig. 12a.

The structural framework is described in relation to the compressional and transitional domains of the DWFTB system in the following subsections as the geometry and displacement characteristics of each domain differ greatly. As explained previously, the Albian (marker 1) and Turonian (marker 2) maximum flooding surfaces are also shale detachment surfaces upon which gravitational slip has occurred during deformation. The majority of all structural framework faults terminate at depth along one of these surfaces and extend upwards to either the early Campanian (marker 4), Oligocene (marker 7), or Miocene (marker 8) sequence boundaries depending on their location with respect to the DWFTB system (Figs. 6, 7 and 8).

4.2.1 Compressional domain

DWFTBs occur down-dip in the compressional domain with slip mainly upon the Turonian seaward-dipping shale detachment surface (marker 2, Figs. 6 and 7). Subtle ramps along this upper shale detachment surface links multiple levels of basal slip well seen in the NW section of Fig. 7. Imbricate thrust faults detach mostly against the Turonian surface (marker 2) with some extending to the Albian surface (marker 1) at depth and fewer continuing to greater depths. Thrust faults terminate either just below or at the early Campanian sequence boundary (marker 4) within the C1 late drift sequence (Figs. 6 and 9). Faults are relatively equally spaced between 1.6–2 km, with average displacements of 250 m. Thrust faults trend in a NW–SE direction (Figs. 5 and 12a, b). They dip on average between 22–45° NE with generally lower dip angles where they detach the Turonian (marker 2) or Albian (marker 1) surfaces at depth (Figs. 9 and 12b, c).

Thrust sheets are crosscut and displaced by extensive oblique-slip normal faults measuring up to ~20 km in length (Figs. 5, 7 and 12a, b). Oblique-slip faults are interpreted to have formed from the combination of tension and shearing during the down-dip contraction of sediment from the transitional to the compressional domain. They show a dip-slip and strike-slip offset of ~80 m and ~200 m, respectively. The oblique-slip faults trend in NE–SW direction and show left-lateral (sinistral) motion. They dip on average between 40–70° NW with few dipping SE in the region of the compressional domain (Figs. 7 and 12a, b, d). In plan section oblique-slip faults display a spoon-shaped geometry (Figs. 5 and 12a, b). The central zone of the spoon-shaped geometry (Figs. 5 and 12a, b) contains a series of smaller ~2 km length normal faults dipping both NW and SE. Some display overlapping or step-like, en-echelon type geometries indicating tensional shear (Fig. 5). The central zone forms a broad anticlinal feature observed to the SE of the anticline noted in the previous section (Fig. 8). The central zone is not as heavily faulted and deformed compared to its outer surroundings. Along-strike, sinistral oblique-slip motion decreases in the direction of the transitional domain (easterly), until only normal dip-slip motion occurs where thrust sheets do not appear to be crosscut (Fig. 5). Vertically, both normal and oblique-slip faults are assumed to have initially terminated at the early Campanian surface (marker 4) detaching at depth along the Turonian surface (marker 2) (as is the case for the thrust faults shown in Figs. 6 and 7). Oblique-slip faults are interpreted to have been reactivated to terminate along or within stratigraphically lower (Albian, marker 1), and higher (Oligocene and Miocene, markers 7 and 8) surfaces and sequences (Figs. 6, 7 and 8).

A deviation from the normal trend of the oblique-slip faults is seen SE of the study area, as shown in Figures 5b and 12a, b, occurring just outside the spoon-shaped region. Here, the oblique-slip faults dip to the W and SE and show right-lateral (dextral) slip motion in contrast to those in the rest of the study area (Figs. 5b and 12a, b). This more structurally complex region has smaller localized sets of fold-and-thrust belts occurring below the kilometre-scale DWFTB system (Figs. 6 and 10). The smaller scale DWFTBs occur within sequence B1, detaching from the Albian surface (marker 1). The smaller set of secondary DWFTBs are less well-defined and weakly folded with smaller thrust spacings of ~250 m and metre-scale displacements compared to those of the overlying kilometre-scale DWFTBs. Similar sets of clear, small-scale DWFTBs are found in other portions of the compressional domain between the Albian (marker 1) and Turonian (marker 2) shale detachment surfaces. In very poorly seismically imaged areas, the mounded and chaotic geometry of basin floor turbidite sediments may be misinterpreted as these smaller-scale DWFTBs due to the loss of seismic resolution with depth.

4.2.2 Transitional domain

The transitional domain is characterized by an extremely complex framework consisting of crosscutting normal, oblique-slip and a few thrust faults (Figs. 5 and 12a, b). There is a gradational change from the central transitional to the down-dip compressional domains. From east to west (in the down-dip direction) we see; a series of opposite-dipping normal faults which then overlap with oblique-slip faults and then finally a few thrust faults (Figs. 5, 6 and 12a, b). Due to deformation, the Turonian shale detachment surface (marker 2) appears irregular and therefore often merges with the Albian shale detachment surface (marker 1) in the transitional domain (Fig. 8at depth, and breaches the Cenozoic sequences to terminate at either the Oligocene or Miocene sequence boundaries (Fig. 8). Erosional features observed in the Cenozoic sequences (Figs. 8 and 11) are confined specifically to the transitional domain (Fig. 5b) for both the Oligocene canyon and Miocene channel-like features (markers 7 and 8, respectively).

Normal faults observed in the study area have a short and discontinuous lateral extent, ranging from 1–13 km at most (Fig. 5). Their vertical extent often goes beyond the Turonian (marker 2) to the Albian shale detachment surface (marker 1) at depth and breaches the Cenozoic sequences to terminate at either the Oligocene or Miocene sequence boundaries (Fig. 8).Normal faults dip ~50–70°, on average, in opposite NW and SE direction and trend NE–SW, perpendicular to the thrust faults (Fig. 5). Along individual fault planes, dip angles as low as ~30° may occur at depth, while the higher dip angles occur in stratigraphically higher sequences (Fig. 12b, d). This along-plane change in dip defines them as listric normal faults. Although the opposite dipping listric normal faults form a few conjugate pairs, it is evident which dip direction dominates between the north and the south of the study area (Figs. 8 and 12a). Usually, the conjugate pair consists of one long, and therefore dominant, fault intersected by a much smaller, opposite-dipping fault as seen in the NE section of the study area (Fig. 12a, b). In Fig. 12a, b the distinction of the more dominant fault directions is evident compared to those seen in the interpretation of the regional seismic sections (Figs. 6, 7 and 8). This is because we only included faults greater than ~2 km in length (laterally) for the structural framework (Fig. 12a, b); whereas most vertically extensive faults, regardless of their lateral length, were interpreted in the 2D seismic sections (Figs. 6, 7 and 8).

Figure 12a shows NW dipping faults dominating in the north, and SE then SW dipping faults dominating in the south. Upon closer inspection, and the use of the variance seismic attribute, it is evident that some faults extend past the lower Albian shale detachment surface (marker 1)in the transitional domain to the lower bounding surface of sequence A in the Early Cretaceous (Fig. 8). Fault displacements in the Late Cretaceous sequences (B2, C1 and C2) may reach ~80 m. In the stratigraphically lower and higher sequences, the magnitude of displacement gradually decreases until the faults are completely terminated. This suggests that deformation due to sedimentary contraction was greatest during the Late Cretaceous causing the Albian shale detachment surface (marker 1) to be the most efficient slip surface after the Turonian surface (marker 2) had reached maximum or considerable strain (Fig. 8). Secondary normal faults (those that originate from a larger fault) are common in the late drift to early Cenozoic megasequences. These attach to the main faults at acute angles with intersections in megasequence C (Fig. 8). Due to their small vertical and lateral extent (< 2 km), they were not included in the structural framework shown in Fig. 12a, b given that this study focusses on the regional scale structures affecting basin evolution.

5 Discussion

5.1 Strato–structural evolution of the deep-water Orange Basin

We present a model explaining the evolution of the deep-water Orange Basin (Fig. 13) using the stratigraphic and structural observations made in the present study, and previous literature on the tectonic history of the basin (e.g., Séranne and Anka, 2005; Paton et al., 2007; Wigley and Compton, 2006; De Vera et al., 2010; Hirsch et al., 2010; Kuhlmann et al., 2010; Scarselli et al., 2016). The following sequence of events is proposed; from the formation of a Late Cretaceous DWFTB system, to its control on overlying Cenozoic sedimentation, as well as the development of mass transport complexes:

a) **~91.5 Ma (Turonian):** margin uplift in the Late Cretaceous caused sea-level fall, and an increase in sedimentation rates (De Vera et al., 2010).

b) **~91.5–88 Ma (Turonian–Coniacian):** listric normal faulting in the up-dip extensional domain led to the formation of fold-and-thrust belts in the down-dip compressional domain (e.g., De Vera et al., 2010; Morley et al., 2011; Dalton et al., 2015), with gravitational collapse being initiated in the central transitional domain (Dalton et al., 2017). Gravitational sliding first occurred along the upper Turonian shale detachment surface (marker 2) where faults initially detach (Fig. 6).

c) **~83 Ma (Santonian–late Campanian):** as deformation continued until the late Campanian, sediments became highly strained, and stress was redistributed through:
    1. The downward propagation of proximal listric normal faults to a lower Albian shale detachment surface (marker 1) (Fig. 8) encouraging gravitational sliding to continue. This led to the formation of smaller scale DWFTBs between the upper and lower shale detachment surfaces in the distal down-dip direction (Figs. 6 and 7).
    2. Concurrent oblique-slip faulting along-strike the thrust sheets, laterally segmenting the deformed Late Cretaceous megasequence (Figs. 5, 7 and 12a,b; Scarselli et al., 2016).

d) **~30 Ma (Oligocene):** a major sea-level fall past the shelf break (Siesser and Dingle, 1981; Siesser and Dingle, 1981; Miller et al., 1995) led to the formation of a large Oligocene canyon as sediments were eroded by a downslope turbidity current (marker 7 in Figs. 8 and 11a, b).

e) **~12–10 Ma (Miocene):** sea-level fall with margin uplift (Hirsch et al., 2010) led to the formation of multiple crosscutting and sinusoidal channels in the Miocene (marker 8 in Figs. 8 and 11c, d) caused by the slope-parallel erosive action of bottom currents possibly related upwelling of the Benguela Current at ~10 Ma (Fig. 3; Diester-Haass et al., 2004; Rommerskirchen et al., 2011).

f) **0 Ma (present):** Slope instability caused present-day slumping of seafloor sediments (Figs. 7 and 9).

Gravitational processes in the Orange Basin have been enhanced by several phases of uplift and denudation, responsible for crustal thinning and the inversion of extensional faults recorded in the SW African margin's Cretaceous post-rift megasequence (Granado et al., 2009; De Vera et al., 2010; Hirsch et al., 2010; Hartwig et al., 2012; Brown et al., 2014; Wildman et al., 2015). The combination of episodic margin uplift and thermal subsidence allowed downslope gravitational sliding and spreading (De Vera et al., 2010). Trigger mechanisms for sediment failure and subsequent gravitational collapse include rapid sedimentation

https://doi.org/10.5194/egusphere-2022-180
Preprint. Discussion started: 10 May 2022

rates with resultant high internal pore fluid pressures, seismicity, downslope undercutting, and tilting glide planes (Séranne and Anka, 2005; Rogers and Rau, 2006; Kuhlmann et al., 2010).

The kinematics, geometry and displacement characteristics of structures seen within the transitional and compressional domains of the DWFTB system imaged in this study differs greatly. We discuss the variability of the two domains imaged to explain the strato-structural evolution of the Orange Basin from a Late Cretaceous DWFTB system to Cenozoic mass transport systems and deposits. To fully understand the evolution of the Orange Basin, it is important to look at the factors that controlled the gravitational collapse, together with the lateral and vertical relationship between the transitional and compressional domains, and their overlying sequences through progressive sedimentation.

5.2 Lateral relationship between the transitional and compressional domains of a Late Cretaceous DWFTB system

Dalton et al. (2017) proposed that the gravitational collapse was initiated in the transitional domain of the Orange Basin upon an unstable slope. In response to up-dip extension, down-dip compression formed landward-dipping imbricate thrust faults with seaward-verging folds in a linked distal domain (Paton et al., 2007; De Vera et al., 2010; Morley et al., 2011; Dalton et al., 2015). Thrust sheets of the compressional domain are displaced by arcuate, concave-upwards oblique-slip faults, laterally extending from the transitional domain with horizontal displacements increasing in the down-dip direction (Figs. 5 and 12a, b, c). In this study, the oblique-slip faults display a spoon-shaped geometry in plan view as was also observed by De Vera et al. (2010) and Scarselli et al. (2016) in other Orange Basin DWFTB systems. Those presented in Scarselli et al. (2016)'s study dipped in opposite N and S directions (towards each other) in contrast to the same NW dipping direction in this study.

The oblique-slip faults are shown to have rotated the Turonian to Santonian (sequence B2) sediments, forming a broad central rollover anticline (Figs. 5 and 7). The difference and changes in slip along each oblique-slip fault reflects the way in which differential movement is accommodated for between the footwall and hanging wall blocks of the thrust sheets (Benesh et al., 2014).

There are two different schools of thought in what the transitional domain represents:

1. A zone caused from the central shift in contact between extensional and compressional tectonics containing overprinted features of both (Butler and Paton, 2010; De Vera et al., 2010). This was proposed due to the crosscutting relationships observed in the distal parts of the extensional domain.
2. A fixed package of mostly undeformed rock representing a short wave-length change from extensional to compressional tectonics (Corredor et al., 2005; Krueger and Gilbert, 2009; Dalton et al., 2017).

We propose that it is a zone comprising overprinted features of both extensional and compressional tectonics since crosscutting relationships are evident (Figs. 5 and 12a, b). In previous Orange Basin studies, the transitional domain was interpreted as a relatively narrow region (~10 km in length perpendicular to the slope) considering the massive extent of a complete (roughly ~220 km) DWFTB system (Corredor et al., 2005; Krueger and Gilbert, 2009; De Vera et al., 2010; Dalton et al., 2017). These observations were made from the margins of more proximal DWFTB systems. It is known that no two DWFTB systems are exactly alike (Morley et al., 2011), and in this study, the transitional domain is much greater than 10 km in length. The true extent of the transitional domain is difficult to constrain because of the absence of a full up-dip extensional domain in study; some portions in the NE section of this study (Figs. 5 and 12a, b) may *already* represent the extensional domain.the study area. Since the transitional domain was interpreted as zone containing overprinted features of both compressional and extensional tectonics, it is inherently difficult to define the clear-cut contact it would have with its up-dip and down-dip counterparts; it is *itself* a contact.

5.3 Vertical relationship between the Late Cretaceous DWFTB system and the overlying Cenozoic megasequence

From the analysis of growth stratal patterns in the extensional domain, De Vera et al. (2010) estimated that the gravitational collapse (leading to DWFTB formation) occurred between the Turonian and Campanian (~90–83 Ma). This correlates to the interpretation made in Section 4.1.2 of this deep-water study; that thrusting and (hence deformation) ended by the end of the late Campanian (marker 5 in Figs. 6 and 7) from the observation of stratal changes in fold geometry (compressional domain).

The episodic nature of gravitational sliding (~90–83 Ma) coupled with high sedimentation rates induced margin instability and fault propagation (De Vera et al., 2010; Scarselli et al., 2016). Thrust faults terminate at the early Campanian surface (marker 4) and at depth detach the Turonian surface (marker 2) (Fig. 6). Very few thrust faults extend past the early Campanian and Turonian surfaces and those that do have been influenced by normal and oblique-slip faulting at the point where they crosscut. Most normal and oblique-slip faults, however, terminate in stratigraphically higher Cenozoic, and stratigraphically lower, Early Cretaceous sequences. Figure 8 is a proximal inline section (transitional domain) showing most normal and oblique-slip faults detaching the Albian surface (marker 1)at depth, terminating at the Maastrichtian surface (marker 6), or Oligocene and Miocene sequence boundaries (markers 7 and 8, respectively). Figure 7 is a distal inline section (compressional domain) showing fewer normal and oblique-slip faults extending past the Campanian surface (marker 4) and Turonian shale detachment surface (marker 2). These two seismic sections (Figs. 7 and 8) illustrate the downslope vertical shortening of faults from the up-dip transitional, to the down-dip compressional domain.

Present-day submarine canyon-channel systems are influenced by the underlying structure and geometry of the basin as we observe how faults in the transitional domain terminate at the Oligocene and Miocene sequence boundaries (markers 7 and 8, respectively in Fig. 8). Clark and Cartwright (2009, 2011) describe a modern example in the eastern Mediterranean Levant Basin where present-day submarine canyon-channel systems are either diverted, deflected, blocked or confined by an underlying DWFTB system. Similarly, in this study we see how faulting from a Late Cretaceous DWFTB system has affected the mass-transport complexes observed in Oligocene and Miocene sediments (Figs. 8, 11 and 13d, e). Cenozoic mass transport complexes are known to form in the more landward portions of mature DWFTB systems, reworking sediment from the upper portions of the extensional domain (e.g., Dalton et al., 2017). In contrast to the mass transport complexes of the Late Cretaceous which formed during high rates of sediment discharge to produce large-scale thrust belt systems, those of the Cenozoic formed during times of low sediment supply along a high initial shelf gradient with decreasing thermal subsidence (Dingle et al., 1983; Kuhlmann et al., 2010).

The Oligocene sequence boundary corresponds to a major, though often controversial, erosional event recognised in literature and seen throughout the African coastline (Fig. 3; Siesser and Dingle, 1981; Siesser and Dingle, 1981; Miller et al., 1995). It was caused by margin uplift and resulted in a relative sea-level fall possibly beyond the shelf break (although controversial) and is evidenced by; tilting topsets in the Walvis Basin, and a 350 m difference in elevation between the Late Eocene and Oligocene shorelines of the northern Orange Basin at ~30 Ma (Hirsch et al., 2010; Baby et al., 2018). Ensuing sea-level regressions of lower amplitudes are implied between the Oligocene and Miocene sequence boundaries (markers 7 and 8 in Fig. 8), with Oligocene erosion occurring within the same canyon as turbidity currents eroded and transported sediment from the continental margin. The Oligocene canyon (marker 7) documented in this study formed directly above and between two existing planes of weakness (Figs. 8 and 13d) and is only found above the buried transitional domain (Fig. 12a). The planes of weakness are opposite-dipping (NW and SE), normal to oblique-slip faults, forming a horst structure above a deep-seated anticline (Fig. 8). Fig. 12a shows that faults did not guide the direction of canyoning downslope (E–W); instead of following the SW trend of the underlying structural framework, the canyon formed in a NW direction (Fig. 11a, b). This may explain why the canyon abruptly terminates without a notable decrease in width (although there was a decrease in its depth) since it was no longer confined above and between the two opposite-dipping existing planes of weakness. The direction of canyoning could have been deflected by a strong north-flowing bottom current. There is however no evidence to support the theory in the present study or in other studies presently.

The smaller sinusoidal, erosional features of the Miocene sequence boundary are confined mainly above the transitional domain and trend parallel to the slope (Fig. 11c, d). Faults that did not terminate along or beneath the Oligocene sequence boundary, terminate at the Miocene sequence boundary (markers 7 and 8, respectively in Figs. 7 and 8) and do not extend further. Omosanya and Alves (2014)'s study offshore SE Brazil demonstrates how vertical fault propagation was hindered by Oligocene and Miocene mass transport complexes as also observed in this study. The slope-parallel erosional features of the Miocene sequence boundary are interpreted to have been formed by subcircular water and/or sediment motions through the action of erosional deep-water bottom currents (Figs. 11c, d and 13e; Shanmugam, 2008). This contrasts with the roughly slope-perpendicular Oligocene canyon turbidity currents as is the case for the Oligocene sequence boundary (Figs. 11a, b and 13d).

A bottom current that remains active over prolonged periods of time (i.e., millions of years) will affect sedimentation on the ocean floor, from the winnowing of fine-grained sediments to large-scale erosion and deposition of coarse-grained sediments

(Shanmugam, 2008; Rebesco et al., 2008). Erosional undercutting formed by bottom currents are mainly preserved as slope-parallel features reflecting the contoured flow of either a thermohaline-, wind-, or tidal-driven (baroclinic currents) deep-water bottom current (Shanmugam, 2008). Temperature and/or salinity differences in bodies of water along the continental slope cause vertically stratified water layers of different densities (pycnocline). Internal waves (which are oscillating gravity waves) form along the interface of the different water layers, and if these waves correspond to periods of tidal movement baroclinic currents will form. Upwelling in the ocean may also cause internal waves (Federiuk and Allen, 1996). We propose the Miocene erosional features to have been formed by a baroclinic bottom current caused by the upwelling of the Benguela Current recognised at ~10 Ma (Fig. 3; Diester-Haass et al., 2004; Rommerskirchen et al., 2011). The Miocene also corresponds to a sea-level lowstand caused by tectonic uplift attributed to the African superswell (Fig. 3; Séranne and Anka, 2005; Wigley and Compton, 2006; Hirsch et al., 2010)

Present day bottom current data from current meters along the SW African coastline's shelf and slope indicate a pole-ward flow parallel to the local bathymetry with a slight off-shelf component (Compton and Wiltshire, 2009). This includes current meters placed along the 1 000 m and 3 000 m water depth contours in the offshore Lüderitz (Namibia) and Cape basins (South Africa), respectively. The pole-ward flow of bottom currents may be strong enough to erode the slope as is the case off Cape Columbine (South Africa) with current speeds of 16.1 cms^{-1}. The slope-parallel channels of the Miocene indicate that current speeds during this time were even greater, strong enough to erode the slope and occurring over a prolonged period of time. Their well-preserved nature may be attributed to a period of low sedimentation rates throughout the deposition of sequence D3 which formed a contourite depositional system (CDS) deposit (Figs. 6 and 8). Many CDS deposits have been discovered in major oceans worldwide whose bottom currents are shown to have largely initiated around the Eocene-Oligocene boundary at ~32 Ma boundary, then later reactivated, or newly formed, in the Miocene (Rebesco et al., 2014). Depositional features of CDSs have been well studied, however their erosional counterparts are poorly documented. Erosional features are usually found adjacent or in association with contourite drifts, or within wide areas of continental slopes (Rebesco et al., 2014).

The Oligocene and Miocene unconformities of the Orange Basin are contemporaneous to the ~28 Ma and ~10 Ma stratigraphic horizons observed in the adjacent Brazilian Barreirinhas Basin by Krueger et al. (2012). The major difference here, however, is that these stratigraphic horizons formed due to a sea-level rise in the SE South Atlantic rather than sea-level fall for the SW African margin. Lastly, present-day slumping is observed on the ocean floor (Figs. 7, 9 and 13) in the study area above a buried Late Cretaceous syncline. Internally, slumps are highly deformed due to their rotational movement upon a concave-upward glide plane (Shanmugam, 2017).

5.4 Multiple shale detachment surfaces

Gravitational sliding occurs once enough overburden material has accumulated in the basin and there is a lack of cohesion along a weak, sloping detachment surface (Rowan et al., 2004; Morley et al., 2011). Two important factors controlling a gravitational collapse within a basin include the stratigraphy of the margin and thickness of the detachment surface (Rowan et al., 2004; Dalton et al., 2017). In the Orange Basin these factors vary due to the presence and distribution of multiple basal overpressured shale detachment surfaces. The shale detachment surface upon which most gravitational slip occurred, and where most faults detach for this study's Late Cretaceous DWFTB system is the Turonian surface (marker 2 in Figs. 6, 7 and 8). Once the detachment surface can no longer accommodate sliding, due to thinning of the detachment surface, or possibly a change in shale overpressures, a DWFTB system will lock and deformation will cease (Dalton et al., 2017).

Trigger mechanisms, such as episodic uplift or seismicity (De Vera et al., 2010; Rogers and Rau, 2006) may renew deformation in the gravitational system with the reactivation of faults. In this study, we propose the proximal listric normal faults from the transitional domain were first to propagate to the lower Albian shale detachment surface (marker 1 in Figs. 6 and 8). This encouraged gravitational sliding to occur upon the stratigraphically deeper and older shale detachment surface and for stress to be redistributed in the highly strained system (Figs. 6, 10 and 13c). As sediment is contracted downslope, moving along the newly formed slip plane of the older shale detachment surface, small-scale DWFTBs will form between the younger and older shale detachments. We see this occurring between stratigraphic the Turonian and Albian shale detachment surfaces (markers 2 and 1, respectively in Fig. 6). The secondary set of DWFTBs formed are smaller in scale since they are confined between the upper Turonian and lower Albian shale detachment surfaces (stratigraphic markers 2 and 1, respectively in Fig. 6). With progressive deformation, the DWFTB system may follow the same process of being locked and renewed with faults penetrating stratigraphically older sediments, provided there are more shale detachment surfaces at depth, and overpressure conditions permit. Other DWFTB systems with more than one shale detachment surface exhibit this behaviour such as those in the Niger Delta (Rowan et al., 2004).

Another factor to consider during gravitational sliding is the ramping of layers linking multiple slip surfaces (Fig. 7). In this study we observe multiple shale detachment surfaces giving rise to a complex range of geometries within and below the kilometre-scale DWFTB system. The Albian (marker 1) and Turonian (marker 2) shale detachment surfaces are proven hydrocarbon source rocks in the Orange Basin (Fig. 3; Van Der Spuy, 2003). Faults are known to act as migration pathways for hydrocarbons (Mahlalela et al., 2021), therefore understanding the relationship between the two shale detachment surfaces and the faults which detach upon them is important to constrain a possible petroleum system.

6 Conclusion

In this study, we provide insight into the kinematics, geometry and displacement characteristics of structures observed in the compressional and transitional domain of a DWFTB system in the Orange Basin. These insights permitted a greater understanding into the mechanisms responsible for deformation, sedimentation and accommodation following gravitational collapse in the Late Cretaceous to Cenozoic megasequences. The major conclusions drawn from this study include:

1) **Multiple shale detachment surfaces give rise to a complex range of geometries and structural styles.**

- If overpressure conditions are conducive, the presence of multiple shale detachment surfaces will encourage the reactivation and downward propagation of faults forming secondary localized sets of fold-and-thrust belts in stratigraphically older sequences.

2) **Stress and strain are constantly redistributed within the hanging wall and footwall blocks of all faults.**
   - Thrust faults are segmented along-strike by extensive oblique-slip faults of variable slip magnitudes allowing the downslope translation of sediment.
   - With progressive sedimentation faults are reactivated to propagate into stratigraphically younger and older stratigraphic sequences of the transitional domain.
3) **The transitional domain is a zone containing overprinted features of both the extensional and compressional tectonics.**
   - Crosscutting relationships of overlapping normal, oblique-slip and thrust faults are evident.
4) **The underlying structural framework and stratigraphy of the Orange Basin has and always will control its evolution.**
   - Cenozoic sedimentation- the large, kilometre-scale erosional component of mass transport complexes only occurs above the transitional domain with faults terminating at their sequence boundaries.
   - Present-day seafloor slumping- occurs above a buried Late Cretaceous syncline.

In summary, the strato-structural evolution of the Orange Basin has been investigated with an in depth look at structures within the structurally complex transitional domain of a DWFTB system which itself is often poorly constrained. This study has shown the difference in structural styles and effects of a Late Cretaceous transitional and compressional domain and how they have influenced mass transport complexes of the Cenozoic.

7 Acknowledgements

We would like to thank the National Research Foundation (NRF) and the Council for Geoscience (CGS) for funding the first author's research. Our thanks are also extended to Shell South Africa for providing the 3D reflection seismic data, and Schlumberger for the Petrel software and support. We are furthermore grateful for the insights Vuyolwethu Mahlalela provided and to our colleagues and friends from the Wits Seismic Research Centre for the scientific discussions had and invaluable inputs provided.

8 References

Aizawa, M., Bluck, B., Cartwright, J., Milner, S., Swart, R., and Ward, J.: Constraints on the geomorphological evolution of Namibia from the offshore stratigraphic record, 12, 337–346, 2000.

Anon: PASA, 2017. Information and oppurtunities brochure, n.d.

Baby, G., Guillocheau, F., Morin, J., Ressouche, J., Robin, C., Broucke, O., and Dall'Asta, M.: Post-rift stratigraphic evolution of the Atlantic margin of Namibia and South Africa: Implications for the vertical movements of the margin and the uplift history of the South African Plateau, Marine and Petroleum Geology, 97, 169–191, https://doi.org/10.1016/j.marpetgeo.2018.06.030, 2018.

Benesh, N. P., Plesch, A., and Shaw, J. H.: Geometry, kinematics, and displacement characteristics of tear-fault systems: An example from the deep-water Niger Delta, 98, 465–482, 2014.

Bolli, H. M., Ryan, W. B. F., Foresman, J. B., Hottman, W. E., Kagami, H., Longoria, J. F., McKnight, B. K., Melguen, M., Natland, J., and Proto-Decima, F.: Cape Basin continental rise sites 360 and 361, 40, 29–182, 1978.

Brown, A. R.: Interpretation of three-dimensional seismic data, Seventh edition., Published jointly by the American Association of Petroleum Geologists and the Society of Exploration Geophysicists, Tulsa, Oklahoma, U.S.A, 646 pp., 2011.

Brown, L. F., Benson, J. M., Brink, G. J., Doherty, S., Jollands, A., Jungslager, E. A. H., Keenan, J. H. G., Muntingh, A., and van Wyk, N. J. S.: Sequence Stratigraphy in Offshore South African Divergent Basins: An Atlas on Exploration for Cretaceous Lowstand Traps by Soekor (Pty) Ltd, AAPG Studies in Geology 41, AAPG, 191 pp., 1995.

Brown, R., Summerfield, M., Gleadow, A., Gallagher, K., Carter, A., Beucher, R., and Wildman, M.: Intracontinental deformation in southern Africa during the Late Cretaceous, 100, 20–41, 2014.

Butler, R. W. H. and Paton, D. A.: Evaluating lateral compaction in deepwater fold and thrust belts: How much are we missing from "nature's sandbox"?, GSAT, 4–10, https://doi.org/10.1130/GSATG77A.1, 2010.

Chopra, S. and Marfurt, K. J.: Seismic attributes — A historical perspective, GEOPHYSICS, 70, 3SO-28SO, https://doi.org/10.1190/1.2098670, 2005.

Chopra, S. and Marfurt, K. J.: Seismic Attributes for Prospect Identification and Reservoir Characterization, Society of Exploration Geophysicists and European Association of Geoscientists and Engineers, 481 pp., https://doi.org/10.1190/1.9781560801900, 2007.

Clark, I. R. and Cartwright, J. A.: Interactions between submarine channel systems and deformation in deepwater fold belts: Examples from the Levant Basin, Eastern Mediterranean Sea, Marine and Petroleum Geology, 26, 1465–1482, https://doi.org/10.1016/j.marpetgeo.2009.05.004, 2009.

Clark, I. R. and Cartwright, J. A.: Key controls on submarine channel development in structurally active settings, Marine and Petroleum Geology, 28, 1333–1349, https://doi.org/10.1016/j.marpetgeo.2011.02.001, 2011.

Clemson, J., Cartwright, J., and Booth, J.: Structural segmentation and the influence of basement structure on the Namibian passive margin, Journal of the Geological Society, 154, 477–482, https://doi.org/10.1144/gsjgs.154.3.0477, 1997.

Collier, J. S., McDermott, C., Warner, G., Gyori, N., Schnabel, M., McDermott, K., and Horn, B. W.: New constraints on the age and style of continental breakup in the South Atlantic from magnetic anomaly data, Earth and Planetary Science Letters, 477, 27–40, https://doi.org/10.1016/j.epsl.2017.08.007, 2017.

Compton, J. S. and Wiltshire, J. G.: Terrigenous sediment export from the western margin of South Africa on glacial to interglacial cycles, Marine Geology, 266, 212–222, https://doi.org/10.1016/j.margeo.2009.08.013, 2009.

Corredor, F., Shaw, J. H., and Bilotti, F.: Structural styles in the deep-water fold and thrust belts of the Niger Delta, Bulletin, 89, 753–780, https://doi.org/10.1306/02170504074, 2005.

Dalton, T. J. S., Paton, Douglas. A., Needham, T., and Hodgson, N.: Temporal and spatial evolution of deepwater fold thrust belts: Implications for quantifying strain imbalance, Interpretation, 3, SAA59–SAA70, https://doi.org/10.1190/INT-2015-0034.1, 2015.

Dalton, T. J. S., Paton, D. A., and Needham, D. T.: Influence of mechanical stratigraphy on multi-layer gravity collapse structures: insights from the Orange Basin, South Africa, Geological Society, London, Special Publications, 438, 211–228, https://doi.org/10.1144/SP438.4, 2017.

De Vera, J., Granado, P., and McClay, K.: Structural evolution of the Orange Basin gravity-driven system, offshore Namibia, 27, 223–237, 2010.

Diester-Haass, L., Meyers, P. A., and Bickert, T.: Carbonate crash and biogenic bloom in the late Miocene: Evidence from ODP Sites 1085, 1086, and 1087 in the Cape Basin, southeast Atlantic Ocean, 19, 2004.

Dingle, R. V.: Large allochthonous sediment masses and their role in the construction of the continental slope and rise off southwestern Africa, Marine Geology, 37, 333–354, https://doi.org/10.1016/0025-3227(80)90109-7, 1980.

Emery, K. O., Uchupi, E., Bowin, C. O., Phillips, J., and Simpson, E. S. W.: Continental margin off Western Africa: Cape St. Francis (South Africa) to Walvis Ridge (South-West Africa), 59, 3–59, 1975.

Federiuk, J. and Allen, J. S.: Model studies of near-inertial waves in flow over the Oregon continental shelf, 26, 2053–2075, 1996.

Granado, P., Vera, J. D., and McClay, K. R.: Tectonostratigraphic evolution of the Orange Basin, SW Africa, 2009.

Hartwig, A., Anka, Z., and di Primio, R.: Evidence of a widespread paleo-pockmarked field in the Orange Basin: An indication of an early Eocene massive fluid escape event offshore South Africa, Marine Geology, 332–334, 222–234, https://doi.org/10.1016/j.margeo.2012.07.012, 2012.

Hirsch, K. K., Scheck-Wenderoth, M., van Wees, J.-D., Kuhlmann, G., and Paton, D. A.: Tectonic subsidence history and thermal evolution of the Orange Basin, Marine and Petroleum Geology, 27, 565–584, https://doi.org/10.1016/j.marpetgeo.2009.06.009, 2010.

Holtar, E. and Forsberg, A. W.: AAPG Memoir 73, Chapter 29: Postrift Development of the Walvis Basin, Namibia: Results from the Exploration Campaign in Quadrant 1911, 2000.

King, R. C. and Morley, C. K.: Wedge geometry and detachment strength in deepwater fold-thrust belts, 165, 268–279, 2017.

Kramer E.A.J., Heck L.: Orange Basin 3D Pre-processing and preSDM 2013. Shell Global Solutions International B.V., Netherlands, Risjswijk, 2014.

Krueger, A. and Gilbert, E.: Deepwater fold-thrust belts: Not all the beasts are equal, 30085, 2009.

Krueger, A., Murphy, M., Gilbert, E., and Burke, K.: Deposition and deformation in the deepwater sediment of the offshore Barreirinhas Basin, Brazil, 8, 1606–1631, https://doi.org/10.1130/GES00805.1, 2012.

Kuhlmann, G., Adams, S., Campher, C., van der Spuy, D., di Primio, R., and Horsfield, B.: Passive margin evolution and its controls on natural gas leakage in the southern Orange Basin, blocks 3/4, offshore South Africa, Marine and Petroleum Geology, 27, 973–992, https://doi.org/10.1016/j.marpetgeo.2010.01.010, 2010.

Light, M. P. R., Maslanyj, M. P., Greenwood, R. J., and Banks, N. L.: Seismic sequence stratigraphy and tectonics offshore Namibia, Geological Society, London, Special Publications, 71, 163–191, https://doi.org/10.1144/GSL.SP.1993.071.01.08, 1993.

Mahlalela, V., Manzi, M. S. D., Jinnah, Z., Bourdeau, J. E., and Durrheim, R. J.: Structural characteristics and 3D seismic detection of gas migration pathways in the deep-water Orange Basin, South Africa, Mar Geophys Res, 42, 8, https://doi.org/10.1007/s11001-021-09428-y, 2021.

Manzi, M. S. D., Durrheim, R. J., Hein, K. A. A., and King, N.: 3D edge detection seismic attributes used to map potential conduits for water and methane in deep gold mines in the Witwatersrand basin, South Africa, GEOPHYSICS, 77, WC133–WC147, https://doi.org/10.1190/geo2012-0135.1, 2012.

Manzi, M. S. D., Hein, K. A. A., King, N., and Durrheim, R. J.: Neoarchaean tectonic history of the Witwatersrand Basin and Ventersdorp Supergroup: New constraints from high-resolution 3D seismic reflection data, Tectonophysics, 590, 94–105, https://doi.org/10.1016/j.tecto.2013.01.014, 2013.

Maselli, V., Kneller, B., Taiwo, O. L., and Iacopini, D.: Sea floor bedforms and their influence on slope accommodation, 102, 625–637, 2019.

Maslanyj, M. P., Light, M. P. R., Greenwood, R. J., and Banks, N. L.: Extension tectonics offshore Namibia and evidence for passive rifting in the South Atlantic, Marine and Petroleum Geology, 9, 590–601, https://doi.org/10.1016/0264-8172(92)90032-A, 1992.

Menzies, M. A., Klemperer, S. L., Ebinger, C. J., and Baker, J.: Characteristics of volcanic rifted margins, in: Volcanic Rifted Margins, Geological Society of America, https://doi.org/10.1130/0-8137-2362-0.1, 2002.

Miller, D. E., Yates, R. J., Jerardino, A., and Parkington, J. E.: Late Holocene coastal change in the southwestern Cape, South Africa, Quaternary International, 29–30, 3–10, https://doi.org/10.1016/1040-6182(95)00002-Z, 1995.

Mohammed, M., Paton, D., Collier, R. E. L., Hodgson, N., and Negonga, M.: Interaction of crustal heterogeneity and lithospheric processes in determining passive margin architecture on the southern Namibian margin, Geological Society, London, Special Publications, 438, 177–193, https://doi.org/10.1144/SP438.9, 2017.

Morley, C. K., King, R., Hillis, R., Tingay, M., and Backe, G.: Deepwater fold and thrust belt classification, tectonics, structure and hydrocarbon prospectivity: A review, Earth-Science Reviews, 104, 41–91, https://doi.org/10.1016/j.earscirev.2010.09.010, 2011.

Nemcok, M., Schamel, S., and Gayer, R.: Thrustbelts: Structural Architecture, Thermal Regimes and Petroleum Systems, 1st ed., Cambridge University Press, https://doi.org/10.1017/CBO9780511584244, 2005.

Omosanya, K. O. and Alves, T. M.: Mass-transport deposits controlling fault propagation, reactivation and structural decoupling on continental margins (Espírito Santo Basin, SE Brazil), Tectonophysics, 628, 158–171, https://doi.org/10.1016/j.tecto.2014.04.045, 2014.

Petroleum Agency South Africa (PASA): Information and opportunities, Petroleum Agency South Africa, Cape Town, South Africa: https://www.petroleumagencysa.com/images/pdfs/Pet_expl_opp_broch_2017bw1.pdf, last access: 31 March 2022.

Paton, D. A., van der Spuy, D., di Primio, R., and Horsfield, B.: Tectonically induced adjustment of passive-margin accommodation space; influence on the hydrocarbon potential of the Orange Basin, South Africa, Bulletin, 92, 589–609, https://doi.org/10.1306/12280707023, 2008.

Paton, Douglas. A., di Primio, R., Kuhlmann, G., van der Spuy, D., and Horsfield, B.: Insights into the Petroleum System Evolution of the southern Orange Basin, South Africa, South African Journal of Geology, 110, 261–274, https://doi.org/10.2113/gssajg.110.2-3.261, 2007.

Randen, T., Monsen, E., Signer, C., Abrahamsen, A., Hansen, J. O., Sæter, T., and Schlaf, J.: Three-dimensional texture attributes for seismic data analysis, in: SEG Technical Program Expanded Abstracts 2000, SEG Technical Program Expanded Abstracts 2000, 668–671, https://doi.org/10.1190/1.1816155, 2000.

Rebesco, M., Camerlenghi, A., and Van Loon, A. J.: Contourite research: a field in full development, 60, 1–10, 2008.

Rebesco, M., Hernández-Molina, F. J., Van Rooij, D., and Wåhlin, A.: Contourites and associated sediments controlled by deep-water circulation processes: State-of-the-art and future considerations, Marine Geology, 352, 111–154, https://doi.org/10.1016/j.margeo.2014.03.011, 2014.

Rogers, J. and Rau, A.: Surficial sediments of the wave-dominated Orange River Delta and the adjacent continental margin off south-western Africa, African Journal of Marine Science, 28, 511–524, https://doi.org/10.2989/18142320609504202, 2006.

Rommerskirchen, F., Condon, T., Mollenhauer, G., Dupont, L., and Schefuss, E.: Miocene to Pliocene development of surface and subsurface temperatures in the Benguela Current system, 26, 2011.

Rowan, M. G., Peel, F. J., and Vendeville, B. C.: Gravity-Driven Foldbelts on Passive Margins, in K. R. McClay, ed., Thrust tectonics and hydrocarbon systems, Bulletin, 82, 157–182, https://doi.org/10.1306/61EECE28-173E-11D7-8645000102C1865D, 2004.

Scarselli, N., McClay, K., and Elders, C.: Seismic geomorphology of cretaceous megaslides offshore Namibia (Orange Basin): Insights into segmentation and degradation of gravity-driven linked systems, Marine and Petroleum Geology, 75, 151–180, https://doi.org/10.1016/j.marpetgeo.2016.03.012, 2016.

Séranne, M. and Anka, Z.: South Atlantic continental margins of Africa: A comparison of the tectonic vs climate interplay on the evolution of equatorial west Africa and SW Africa margins, Journal of African Earth Sciences, 43, 283–300, https://doi.org/10.1016/j.jafrearsci.2005.07.010, 2005.

Shanmugam, G.: Chapter 5 Deep-water Bottom Currents and their Deposits, in: Developments in Sedimentology, vol. 60, Elsevier, 59–81, https://doi.org/10.1016/S0070-4571(08)10005-X, 2008.

Shanmugam, G.: Global case studies of soft-sediment deformation structures (SSDS): Definitions, classifications, advances, origins, and problems, Journal of Palaeogeography, 6, 251–320, https://doi.org/10.1016/j.jop.2017.06.004, 2017.

Siesser, W. G. and Dingle, R. V.: Tertiary sea-level movements around southern Africa, 89, 83–96, 1981.

Silva, C. C., Marcolino, C. S., and Lima, F. D.: Automatic fault extraction using ant tracking algorithm in the Marlim South Field, Campos Basin, 5, 2005.

Van Der Spuy, D.: Aptian source rocks in some South African Cretaceous basins, Geological Society, London, Special Publications, 207, 185–202, https://doi.org/10.1144/GSL.SP.2003.207.10, 2003.

Van Der Spuy, D., Sayidini, B.: Offshore Namibia discovery signals bright future for South Africa oil and gas, AAPG Explorer: https://explorer.aapg.org/story/articleid/62613/offshore-namibia-discovery-signals-bright-future-for-south-africa-oil-and-gas, last access: 31 March 2022.

de Vera, J., Granado, P., and McClay, K.: Structural evolution of the Orange Basin gravity-driven system, offshore Namibia, Marine and Petroleum Geology, 27, 223–237, https://doi.org/10.1016/j.marpetgeo.2009.02.003, 2009.

Widess, M. B.: How thin is a thin bed?, 38, 1176–1180, 1973.

Wigley, R. A. and Compton, J. S.: Late Cenozoic evolution of the outer continental shelf at the head of the Cape Canyon, South Africa, Marine Geology, 226, 1–23, https://doi.org/10.1016/j.margeo.2005.09.015, 2006.

Wildman, M., Brown, R., Watkins, R., Carter, A., Gleadow, A., and Summerfield, M.: Post break-up tectonic inversion across the southwestern cape of South Africa: New insights from apatite and zircon fission track thermochronometry, Tectonophysics, 654, 30–55, https://doi.org/10.1016/j.tecto.2015.04.012, 2015.

Yilmaz, Ö.: Seismic data analysis: Processing, inversion, and interpretation of seismic data, Society of exploration geophysicists, 2001.

Table 1: Acquisition parameters of the seismic survey (Kramer and Heck, 2014).

Recording	
Recording format	SEG-D
Record length	7168 ms
Recording filter delay	None
Sample rate	2 ms
Low cut filter hydrophone, slope	4.4 Hz, 12 dB / octave
Low cut filter geophone, slope	Not applicable
High cut filter both, slope	214 Hz, 341 dB / octave
Source	
Source type	Dual source
Number of source arrays	2
Number of sub-arrays	3
Shot point interval	25 m (flip/flop)
Array separation	100 m
Array length	15 m
Source volume	4100 cu in
Number of airguns / arrays	30
Operating pressure	2000 psi
Source depth	8 m
Nominal CMP fold	80
Sercel SSAS Sentinel, Sercel Seal-428	
Number of streamers	8
Group interval	12.5 m
Group length	12.5 m
Number of hydrophones / groups	1
Number of geophones / groups	1
Streamer length	7950 m
Streamer separation	200 m
Number of groups / streamers	636
Streamer depth	10–15 m linear slant
Nearest offset	222 m

Table 2: Processing workflow of the seismic survey (Kramer and Heck, 2014).

	Dolphin Geophysical Polar Duchess team
1	Conversion from SEG-D and navigation merge
2	Output to SEG-Y
	Global Processing team
3	Conversion from SEG-Y to Shell's proprietary software (SIPMAP) format
4	Spherical spreading correction
5	Despike
6	Swell noise attenuation
7	Resample to 4 ms
8	Denoise
9	Linear noise attenuation
10	Deghosting
11	Seismic interference attenuation
12	Zero phasing
13	2D surface rendered multiple elimination (SRME) prediction
14	3D SRME prediction
15	LSQ matched subtraction
16	Multiplicity scaling for Kirchhoff migration
17	Phase deabsorption
18	Residual moveout (RMO) analysis
19	RMO velocity model inversion and anisotropy scanning
20	Pre-migration signal enhancement
21	Kirchhoff prestack migration
22	Residual radon demultiplex
23	Amplitude deabsorption
24	RMO correction
25	(Angle) stack
26	Time variant scaling (additional output volumes)
27	Archiving

Table 3: Summary of observations and interpretations made for the key stratigraphic markers and sequences identified in the Orange Basin study.

Stratigraphic marker			**Age (Ma)**	**Seismic sequence**		**Observations**	
This study		**Past studies** (Brown et al., 1995) (Baby et al., 2018)				**Transitional domain**	**Compressional domain**
9	Seafloor	Seafloor	0	Cenozoic		---	
					D3	aggradation; low amplitudes	
						eroded; contourites	--------------------
8	Miocene	Miocene	10-12			erosive unconformity	
					D2	aggradation; low amplitudes, turbidite deposits	
7	Oligocene	Oligocene	30-25			erosive unconformity	
					D1	retrogradation; low amplitudes, truncated	
						downlap 22At1	--------------------
6	Maastrichtian	22At1	67	late drift		maximum flooding surface; truncated	
					C3	aggradation; very high amplitudes	
5	late Campanian	18At1	77.5			maximum flooding surface	
					C2	aggradation; high frequency, high amplitudes	
						--------------------	weakly folded/ parallel
4	early Campanian	17At1	80			erosive unconformity	
					C1	aggradation; low amplitudes	
						sagging, onlap Coniacian	folded, conformable
3	Santonian	16Dt1	85			maximum flooding surface	
					B2	aggradation; low to medium amplitudes	
						normal faults, thrusts	folded and thrusted
2	Turonian	15At1	93			maximum flooding surface, shale detachment	
					B1	aggradation; low to medium amplitudes	
						basin-floor fan deposits	localized folds and thrusts
1	Albian	14At1	103	early drift		maximum flooding surface, shale detachment	
					A	aggradation; low to medium amplitudes	

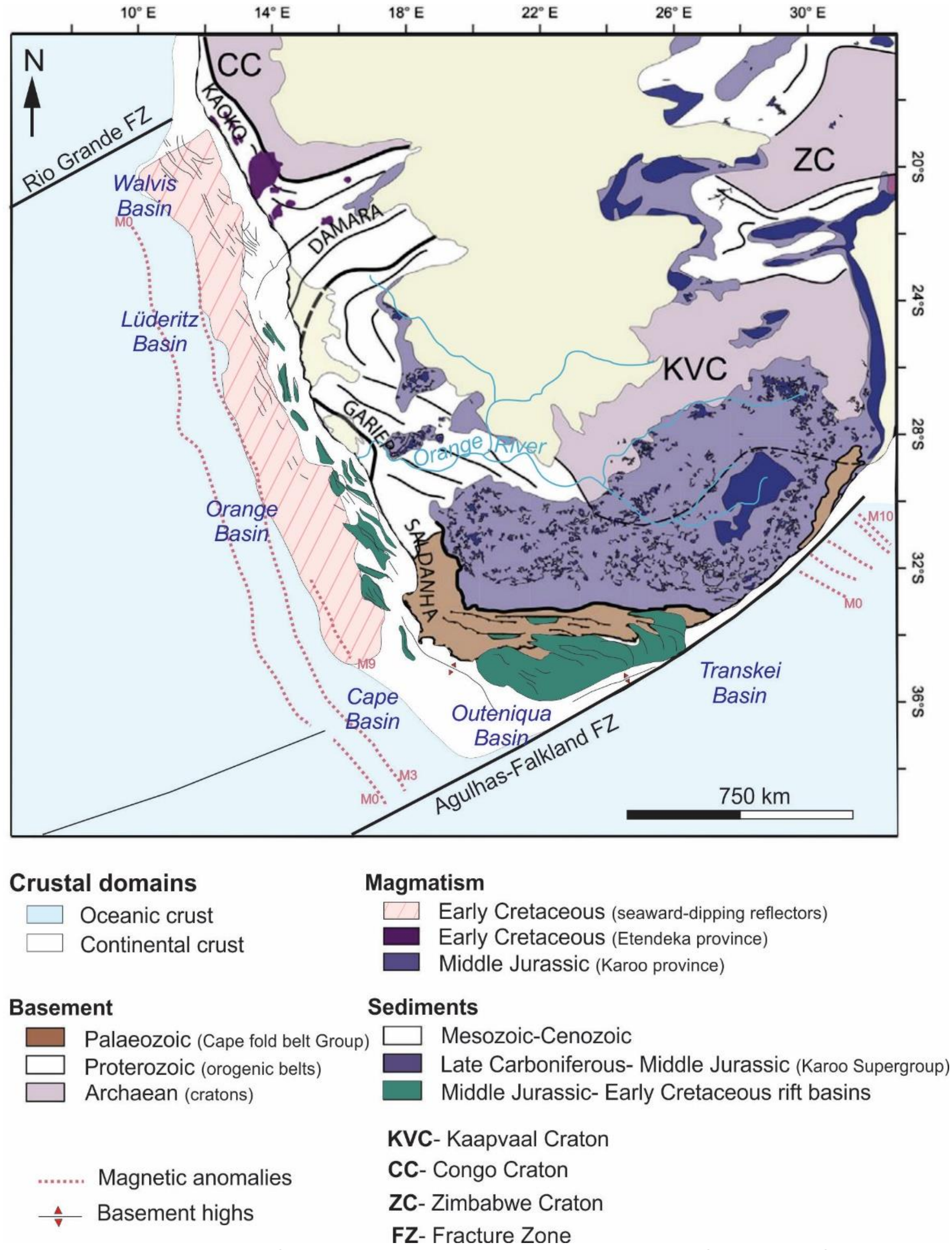

Figure 1: Tectonic structural framework showing the crustal components of southern Africa and major basinal depocentres offshore the SW African margin (adapted from Baby et al., 2018).

]

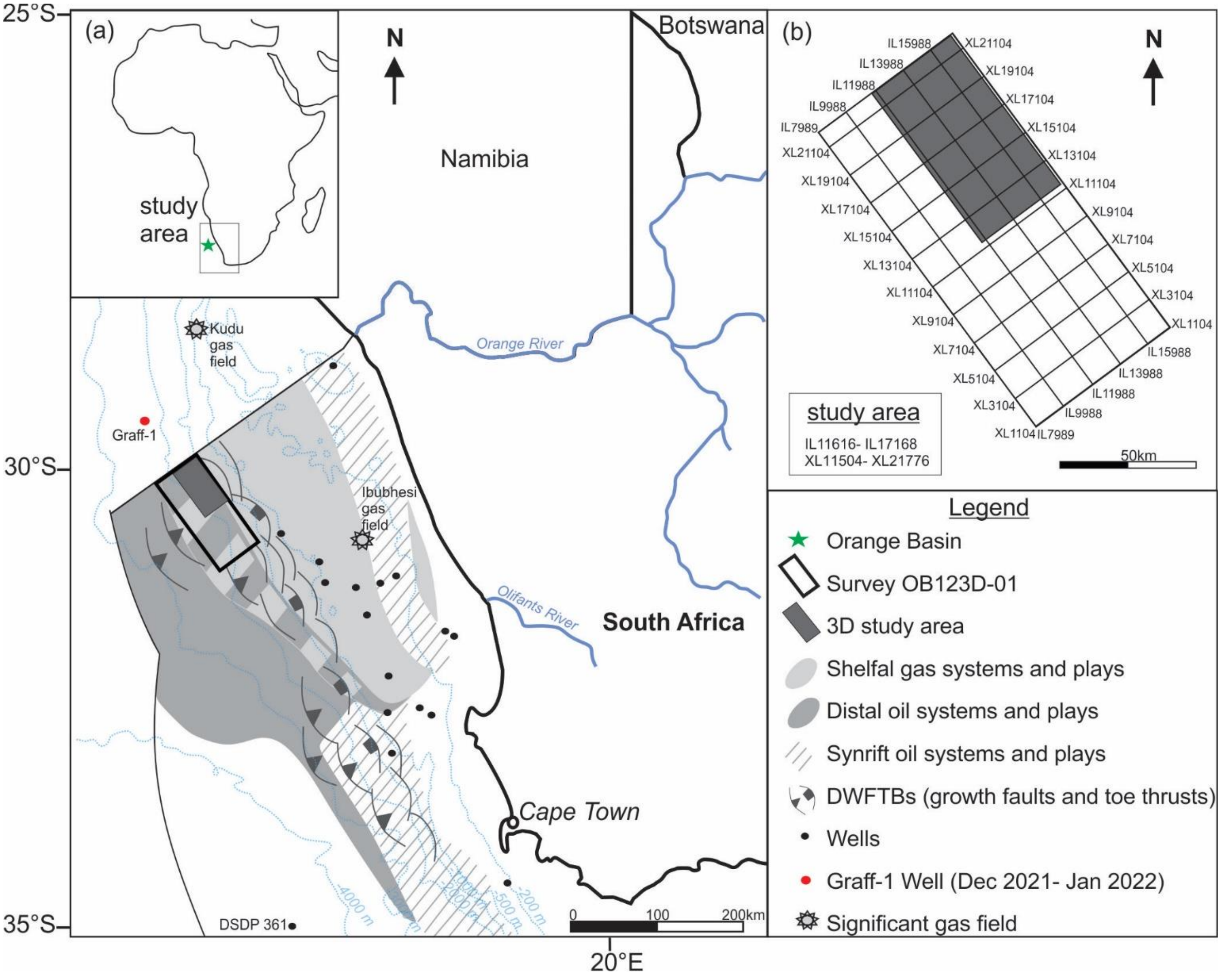

Figure 2: Simplified map of the Orange Basin study area offshore the SW African coastline. (a) Known and predicted petroleum systems and plays, and the position of gravitational structures and wells within the South African licensing area (adapted from Jungslager, 1999). (b) Location of the present study within the full 3D seismic survey 755

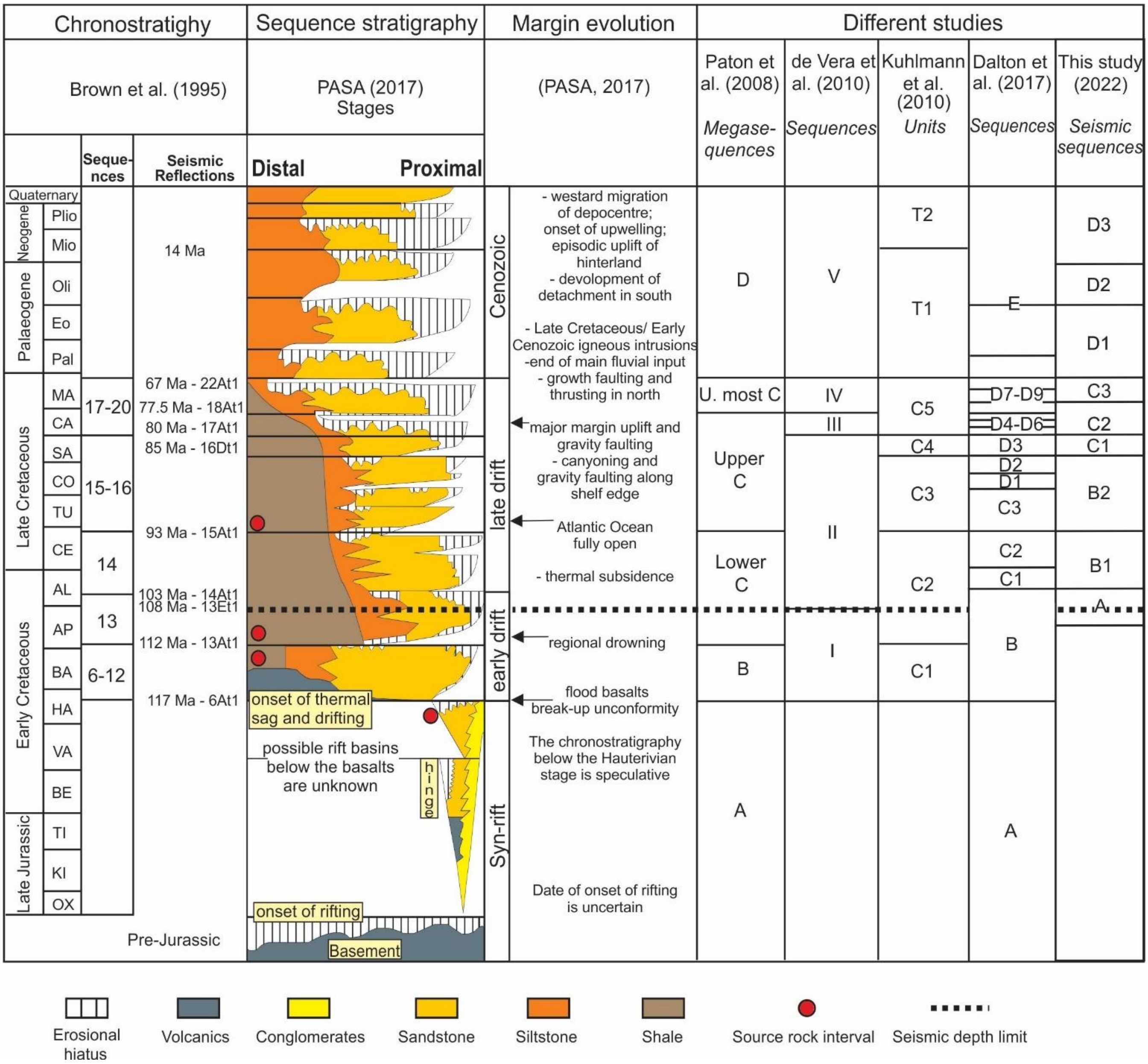

Figure 3: Tectonochronostratigraphic chart of the Orange Basin showing the major depositional sequences, their bounding surfaces, and the evolution of the margin through fluctuations in global and local sea level .

https://doi.org/10.5194/egusphere-2022-180
Preprint. Discussion started: 10 May 2022

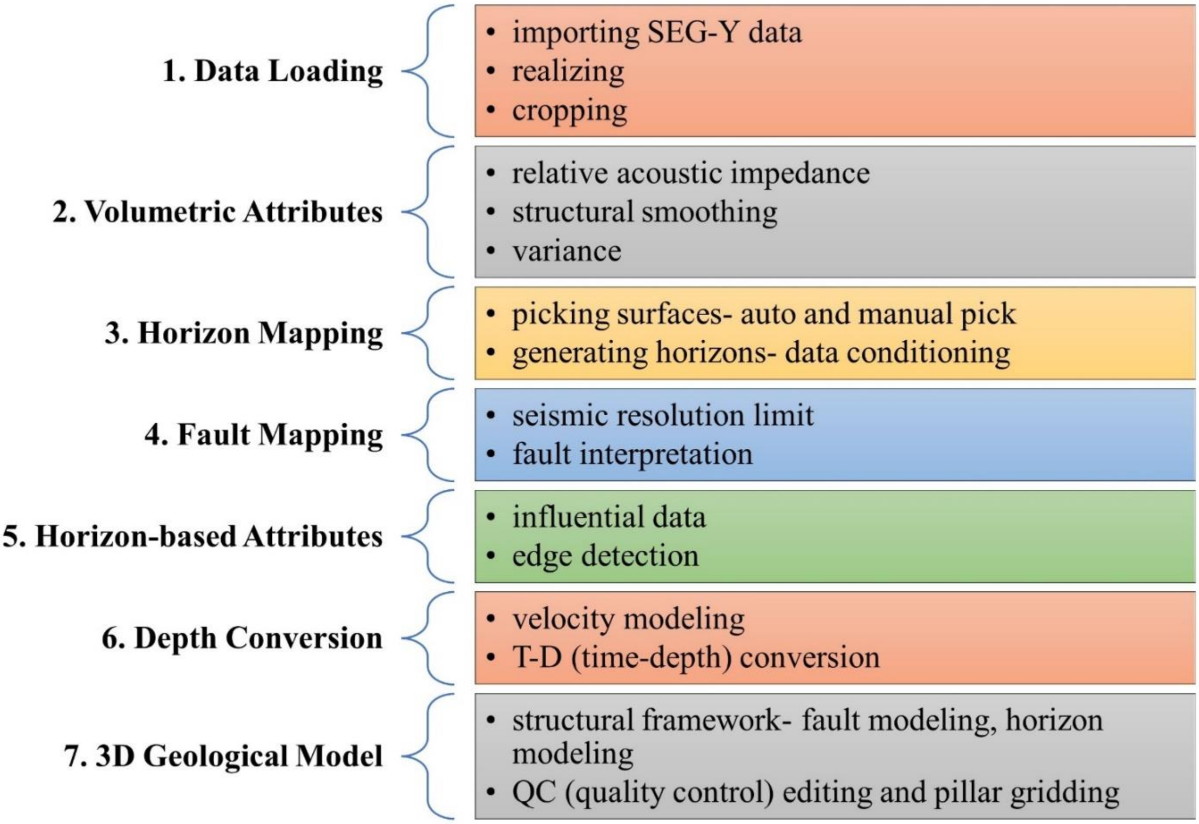

Figure 4: Interpretation workflow used to build this study's geological model using Schlumberger's Petrel software.

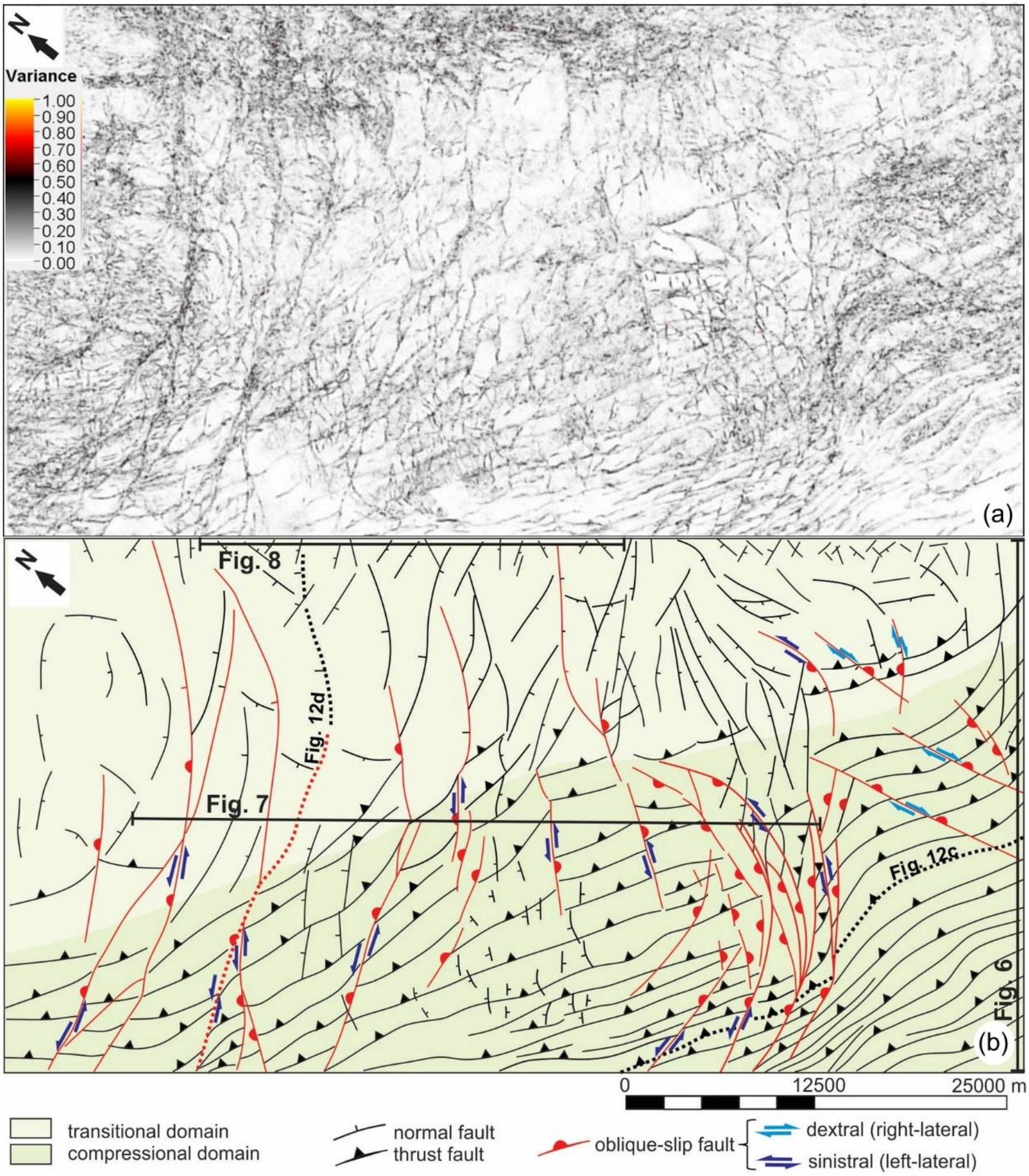

Figure 5: Structural framework showing the transitional and compressional domains imaged in the study area. (a) Uninterpreted variance time slice at -3 424 ms (imaged within sequence B2 covering depths approximately between -3 200 m to -5 000 m) showing the fault continuities. (b) Interpretation of the structural framework including oblique-slip displacement characteristics with the location of regional seismic sections.

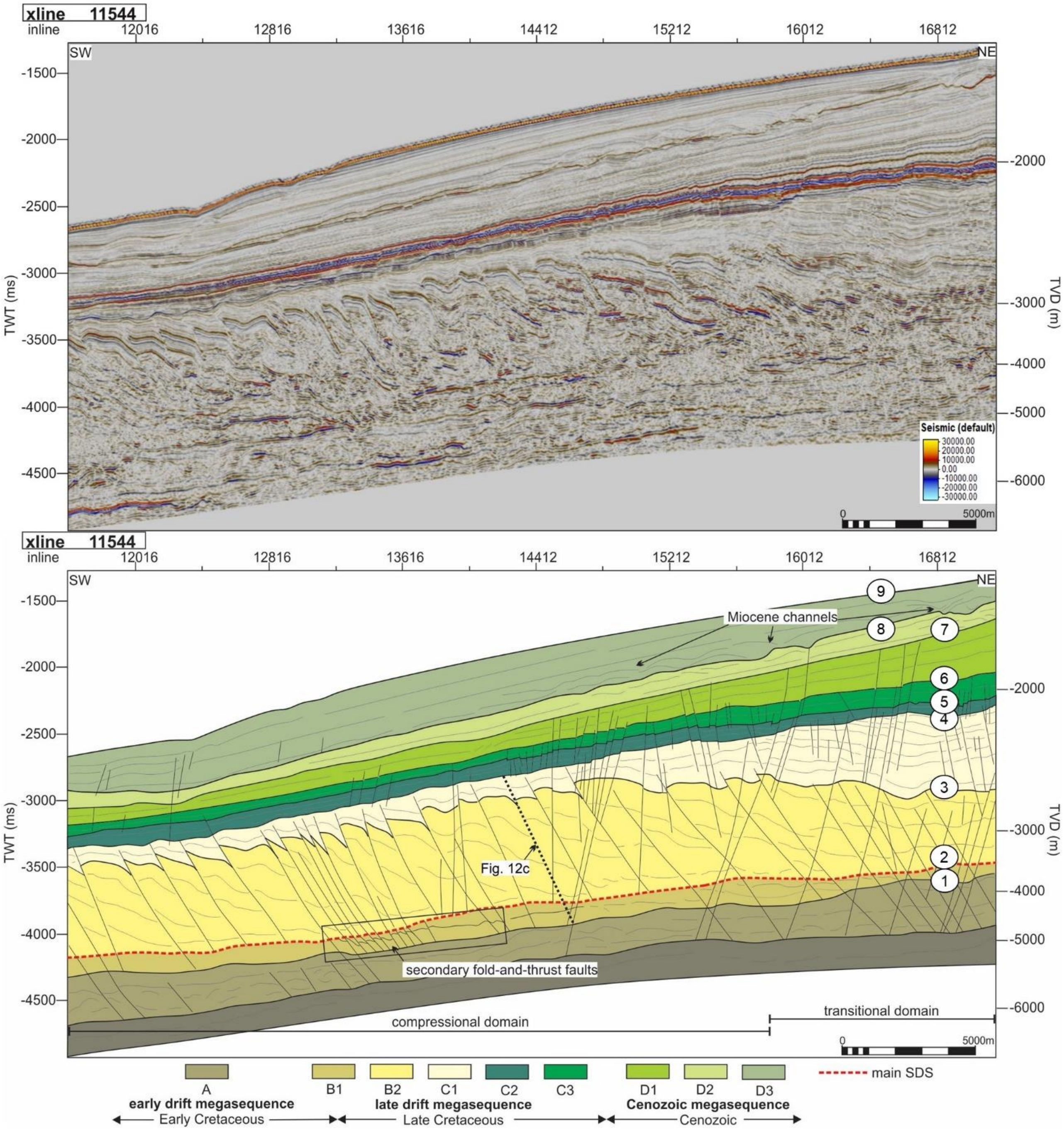

Figure 6: Uninterpreted and interpreted sections of crossline 11544 showing a portion of the transitional and compressional domains. The crossline lies roughly perpendicular to the compressional domain DWFTBs giving a view of their structure in comparison to the transitional domain. Abbreviations: SDS= shale detachment surface, 1= Albian, 2= Turonian, 3= Santonian, 4= early Campanian, 5= late Campanian, 6= Maastrichtian, 7= Oligocene, 8= Miocene, 9= seafloor. Vertical exaggeration= 5.

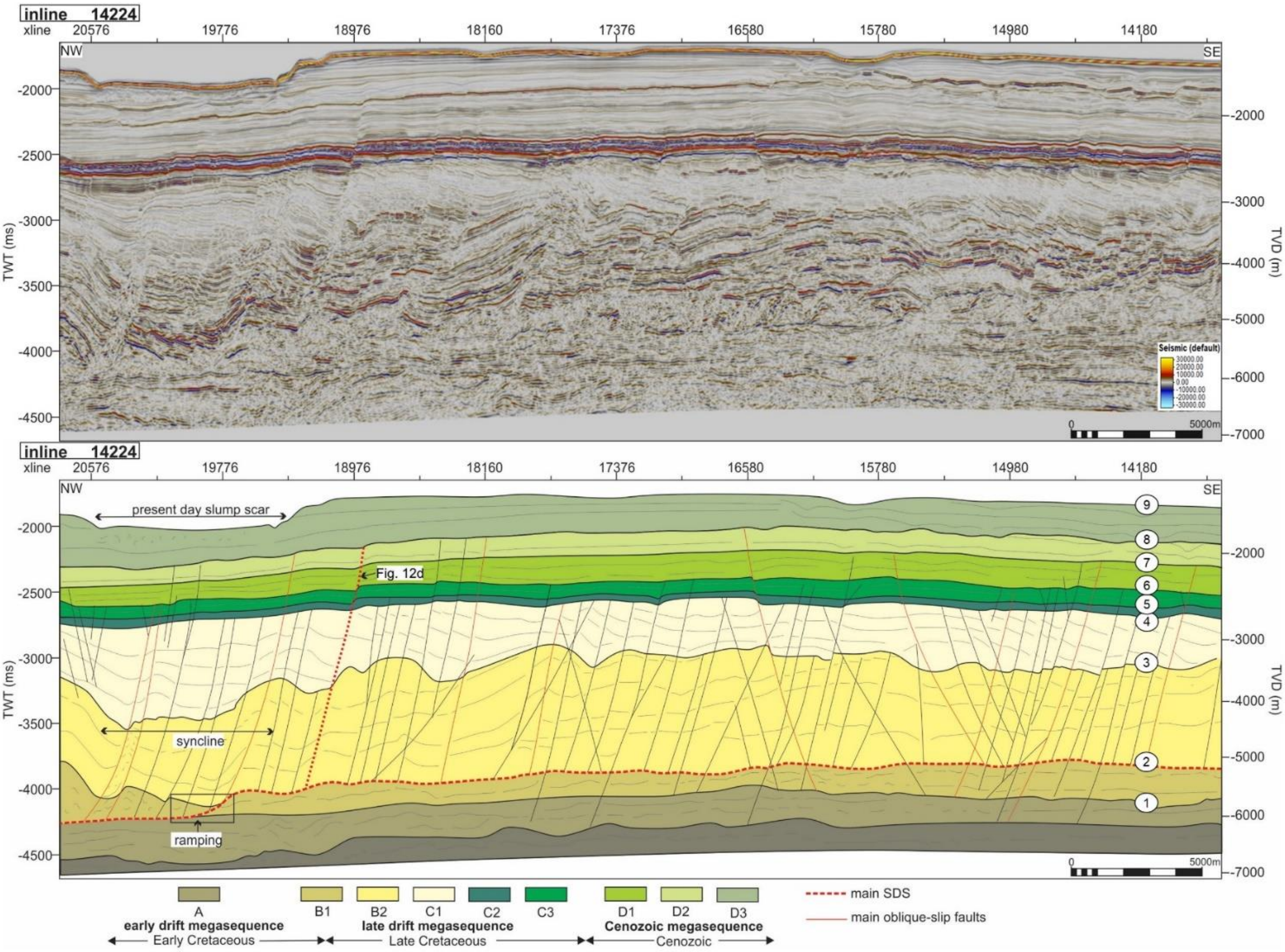

Figure 7: Uninterpreted and interpreted sections of inline 14224 showing the compressional domain. The section lies roughly along-strike the DWFTBs giving a view of the oblique-slip faults that crosscut them. Present day slumping is evident above a Late Cretaceous syncline. Abbreviations: SDS= shale detachment surface, 1= Albian, 2= Turonian, 3= Santonian, 4= early Campanian, 5= late Campanian, 6= Maastrichtian, 7= Oligocene, 8= Miocene, 9= seafloor. Vertical exaggeration= 5.

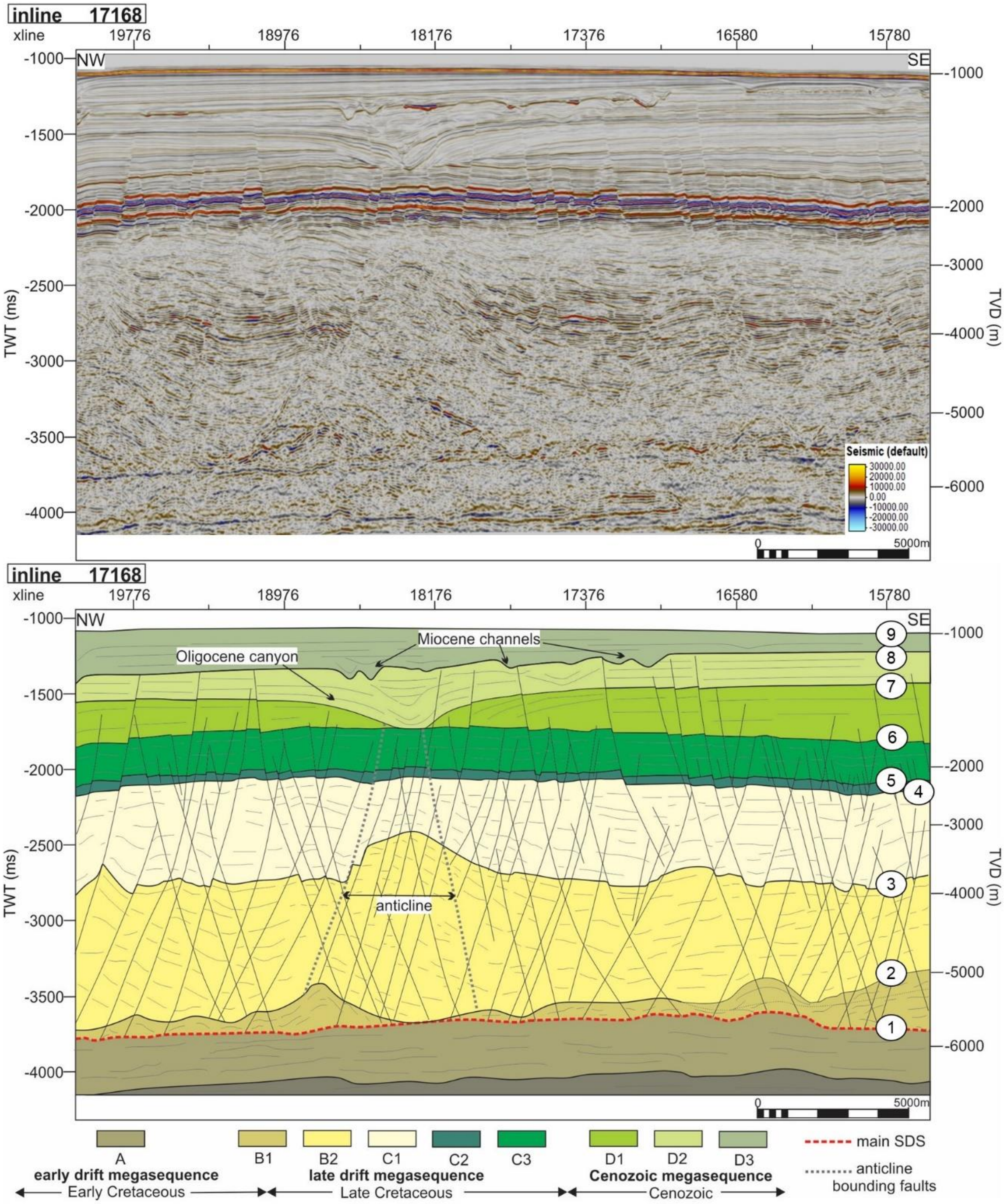

Figure 8: Uninterpreted and interpreted sections of inline 17168 showing the transitional domain. Normal faults extend to surface 1 (the Albian SDS) at depth and upwards into the Cenozoic megasequence with some terminating at unconformity surfaces 7 (Oligocene) or 8 (Miocene). Abbreviations: SDS= shale detachment surface, 1= Albian, 2= Turonian, 3= Santonian, 4= early Campanian, 5= late Campanian, 6= Maastrichtian, 7= Oligocene, 8= Miocene, 9= seafloor. Vertical exaggeration= 5.

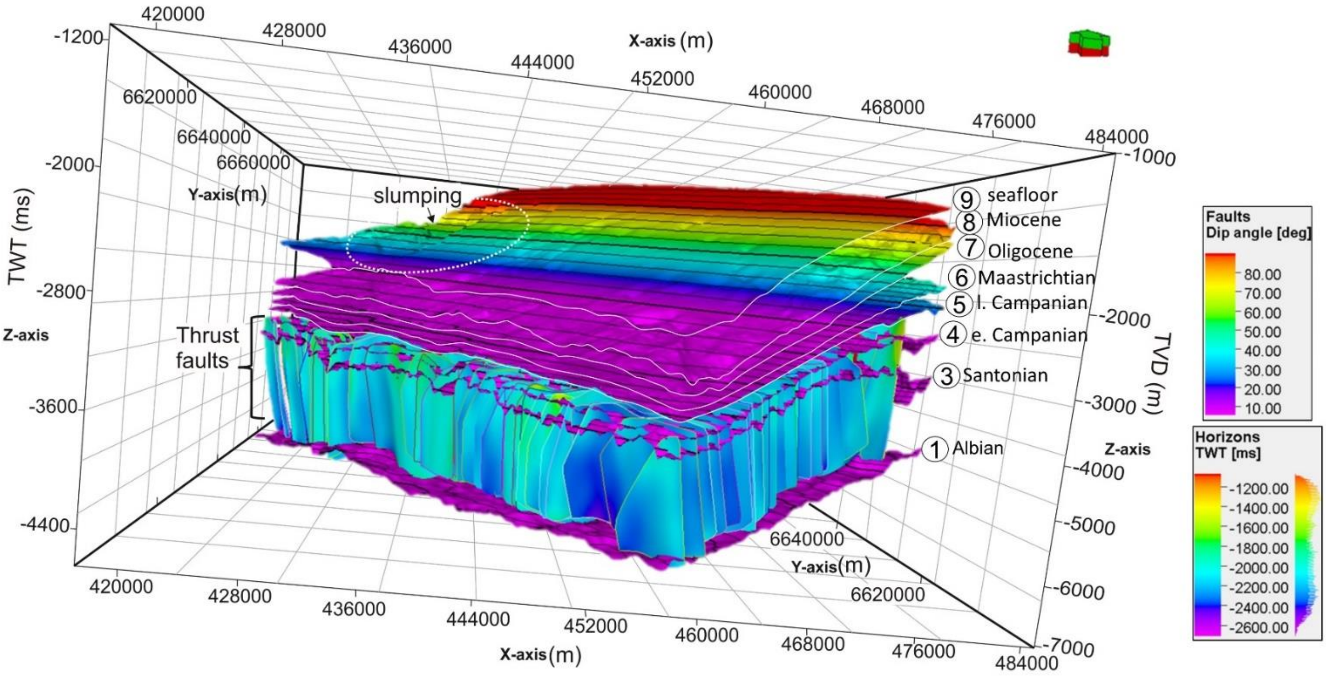

Figure 9: 3D view showing all horizons in TWT (ms), and the dip of all thrust faults interpreted in the study area. Abbreviations: e= early, l= late. Vertical exaggeration= 10.

https://doi.org/10.5194/egusphere-2022-180
Preprint. Discussion started: 10 May 2022

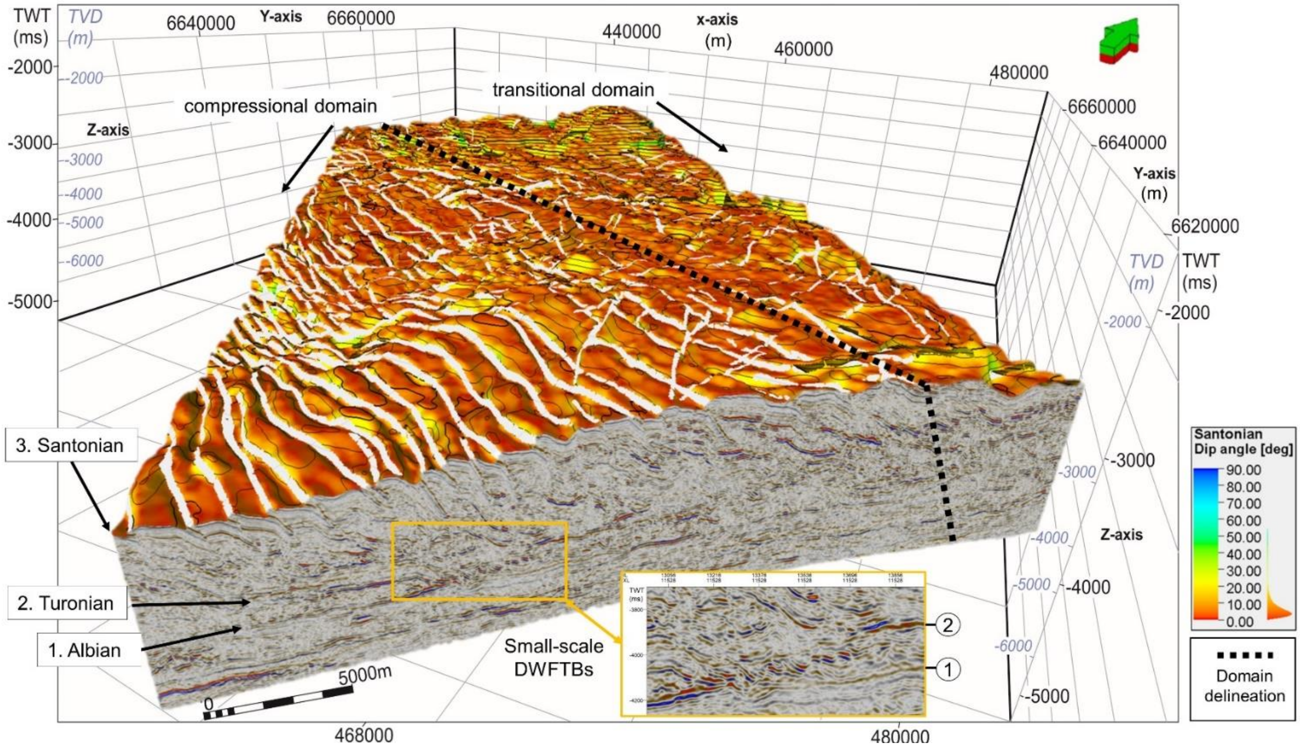

Figure 10: 3D view of a crossline showing; an extensive, kilometre-scale DWFTB system detaching the Turonian slip surface, the Santonian horizon (in dip angle) defining the crest of the large folds, and an underlying localized set of secondary, small-scale DWFTBs upon the Albian slip surface. Vertical exaggeration= 5.

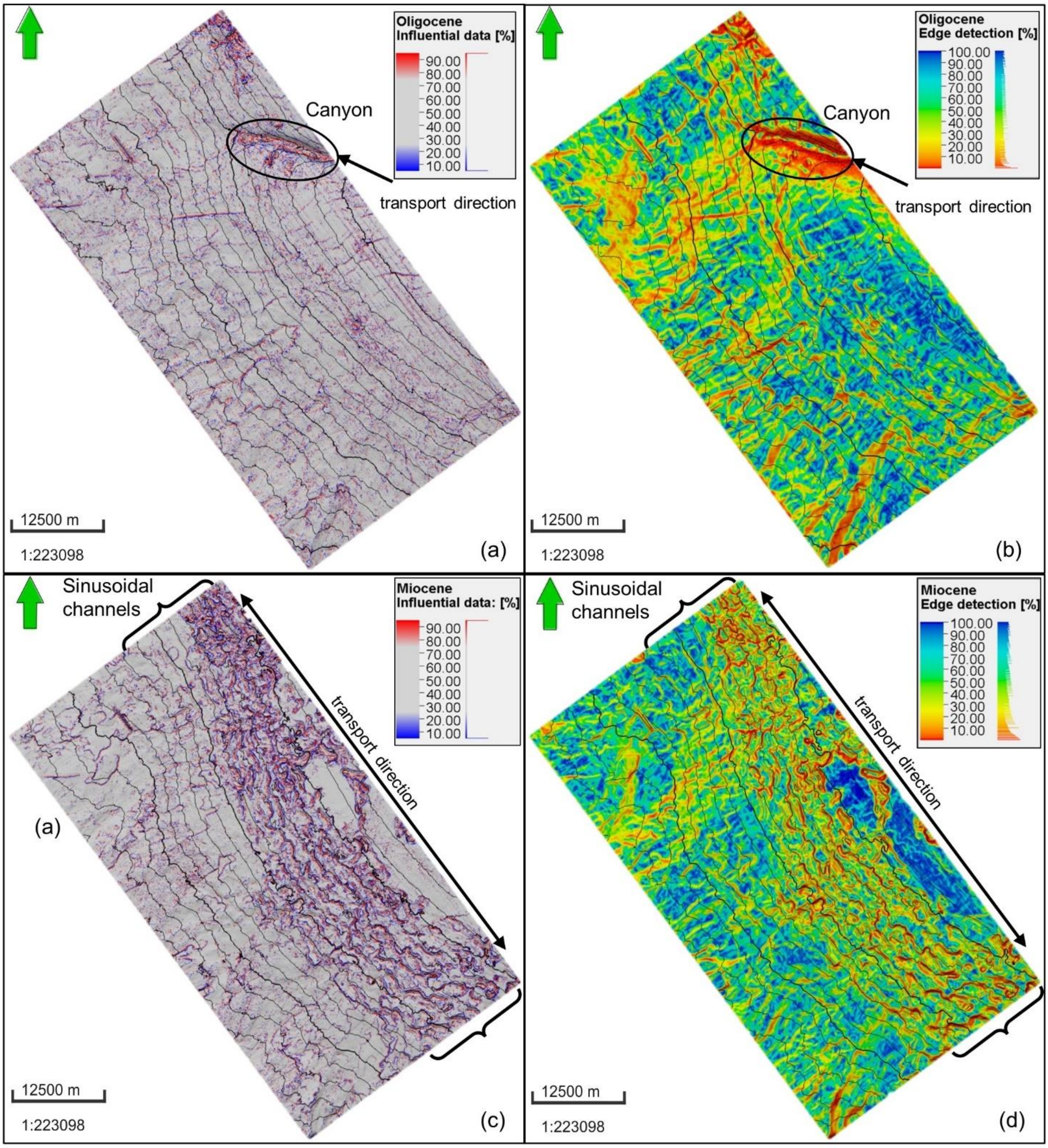

800 **Figure 11: Cenozoic horizons showing the canyon-channel systems. Oligocene canyon formed by a downslope turbidity current viewed using the (a) influential data and (b) edge detection attributes. Miocene sinusoidal channels formed by an along-strike bottom current viewed using the (c) influential data and (d) edge detection attributes. Vertical exaggeration= 5.**

https://doi.org/10.5194/egusphere-2022-180
Preprint. Discussion started: 10 May 2022

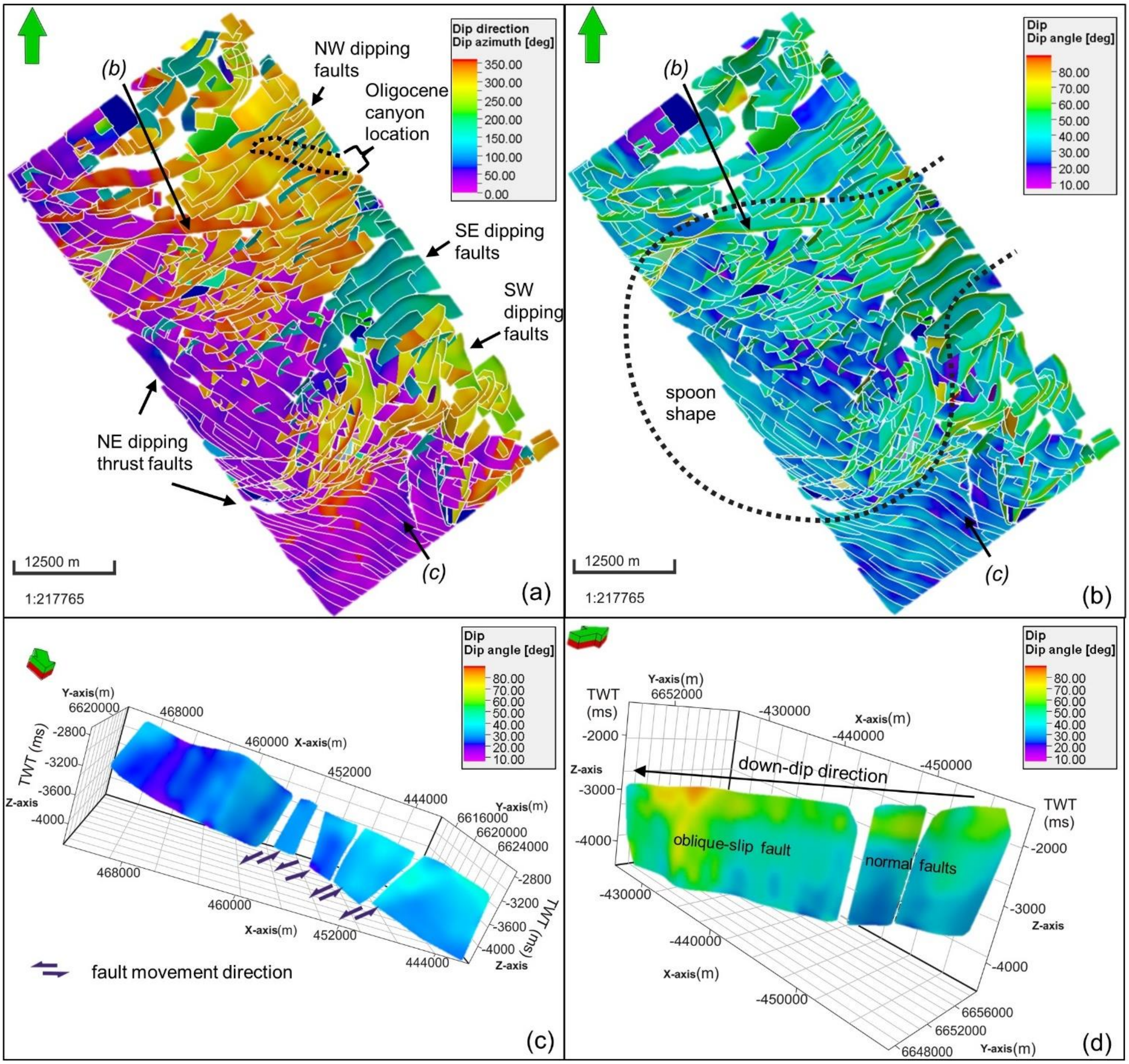

Figure 12: Structural framework faults interpreted in the study area showing: (a) plan view of all the different dip directions between thrust faults and normal and oblique-slip faults using the dip azimuth attribute; (b) plan view the gently dipping thrust faults, and the spoon-shaped geometry of the outer bounding oblique-slip faults; (c) segmented thrust fault using the dip angle attribute (referenced in Fig. 5b); (d) 3D view of an oblique-slip fault and normal faults using the dip angle attribute (referenced in Fig. 5b)

https://doi.org/10.5194/egusphere-2022-180
Preprint. Discussion started: 10 May 2022

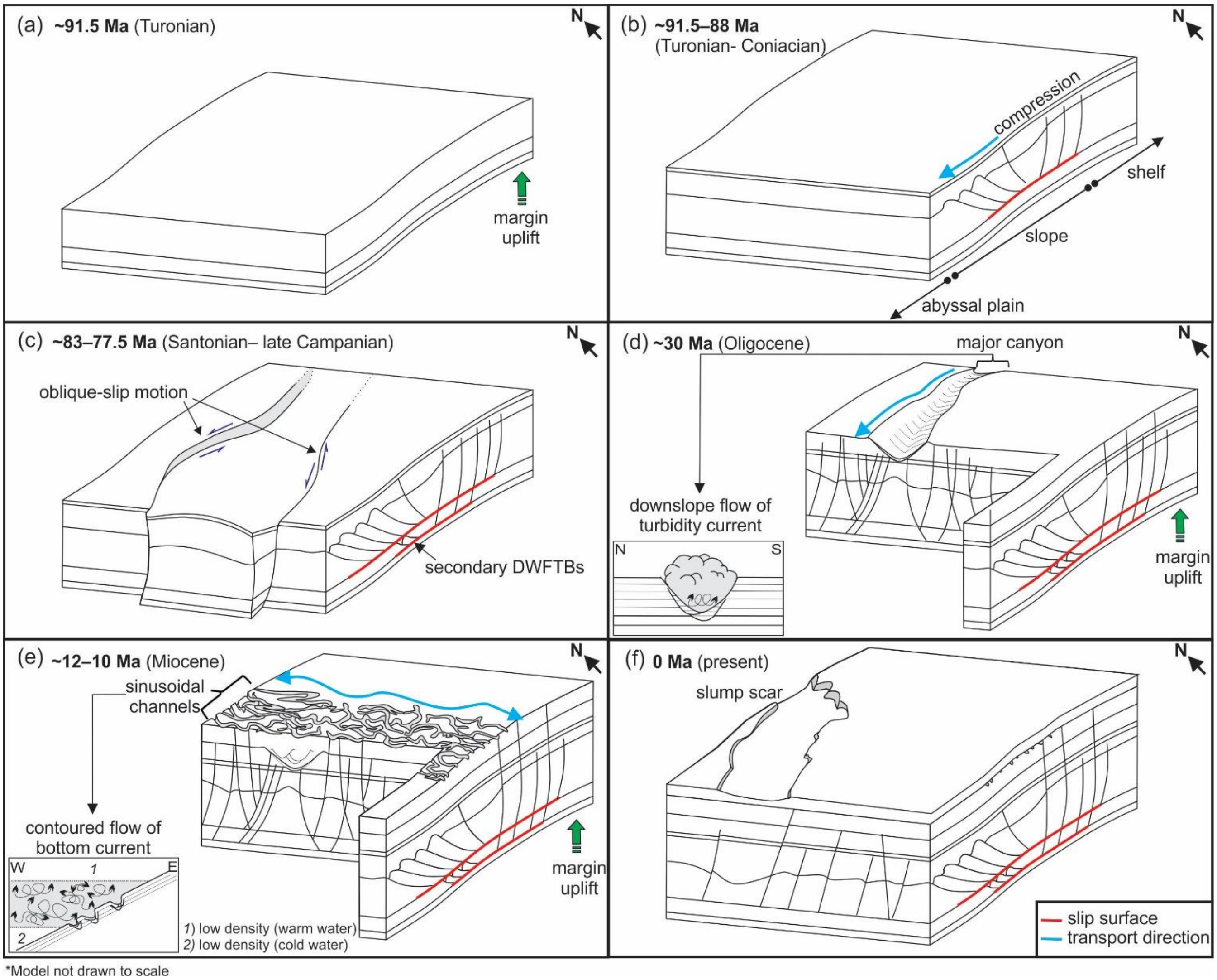

810

Figure 13: Temporal model of the evolution of the deep-water Orange Basin from the Late Cretaceous DWFTB system to the mass-transport complexes of the Cenozoic. For a detailed explanation the reader is referred to Section 5.

815